Università degli Studi di Firenze

DOTTORATO DI RICERCA IN
Scienze Fisiologiche e Nutrizionali

CICLO XXV°

COORDINATORE Prof. *Poggesi Corrado*

Kinetics and mechanics of myosin motors from frog skeletal muscle

Settore Scientifico Disciplinare BIO/09

Dottorando
Dott. *Melli Luca*

_____
(firma)

Tutore
Prof. *Lombardi Vincenzo*

_____
(firma)

Anni 2010/2012

A mia nonna Adele

Acknowledgements

Innanzitutto vorrei ringraziare mia madre e il suo compagno Fabrizio per il loro continuo supporto che mi ha permesso di vivere l'esperienza del dottorato con la massima serenità.

Ringrazio il Prof. Vincenzo Lombardi per avermi dato la possibilità di svolgere il dottorato nel suo laboratorio e per avermi supportato e incoraggiato nei momenti più difficili. Il suo entusiasmo e la sua esperienza sono stati fondamentali per il mio lavoro.

Ringrazio la Prof.ssa Gabriella Piazzesi per avermi aiutato nella stesura di questa tesi.

Ringrazio tutti gli altri membri del Laboratorio di Fisiologia del dipartimento di Biologia di Firenze per avermi supportato e sopportato durante gli ultimi tre anni. In particolare vorrei ringraziare il Dott. Luca Salvi e la Dott.ssa Giulia Falorsi che hanno condiviso con me gioie e amarezze di questa esperienza. Senza il loro aiuto non avrei ottenuto i risultati che ho ottenuto.

Ringrazio la Dott.ssa Manuela Maffei per gli utilissimi consigli per la preparazione delle miosine.

Ringrazio il Dott. Dan Cojoc e tutti i membri del suo laboratorio per il loro fondamentale contributo al mio lavoro di tesi.

I would like to thank Prof. Michael A. Geeves of the University of Kent for giving me the opportunity to work in his lab and all the other members of the lab for their kindness and hospitality that made me feel at home during the three months I spent in England.

Infine, un immenso grazie a Estefania che negli ultimi tre anni ha condiviso con me ogni momento, gioendo assieme a me dei miei successi e consolandomi nei momenti più difficili.

Grazie a tutti!!!!!!!

Luca

INDEX OF CONTENTS

Summary

The work reported in this thesis describes the protocols developed for the realisation of a synthetic sarcomere like machine (MYOMAC) consisting of a single actin filament interacting with a linear array of motor proteins regularly distributed on an inorganic nano-structured surface. The mechanical output of the bio-machine will be measured through a Dual Laser Optical Tweezers (DLOT, range 0.5-200 pN, force, and 1-10,000 nm, displacement). The correct polarity of the actin filament (5-15 μm long) is controlled by attaching its barbed end to a trapped bead *via* gelsolin protein. The motor protein chosen for MYOMAC is myosin from frog skeletal muscle because this is the myosin with the most reliable reference values of mechanical, kinetic and energetic parameters provided by *in situ* studies on intact fibres from frog skeletal muscle. The protocols for the preparation of fully functional myosin II from frog skeletal muscle, recently established in the Laboratory of Physiology of Florence, have been further refined to produce its proteolytic fragments, HeavyMeroMyosin (HMM) and Subfragment1 (S1), to be used in the myosin-based machine. S1 has been characterized in transient kinetic experiments using a stopped flow apparatus. As expected for a fast myosin isoform, frog S1 showed a large rate constant for actin-myosin dissociation by ATP (k_{+2} ~500 s^{-1}, $1/K_1$ ~850 μM at 5°C) and a low ADP affinity (K_{ADP} ~700 μM at 5°C). HMM has been characterized using the *In Vitro* Motility Assay (IVMA). The sliding velocity of actin filaments (V_F) on HMM dispersed on a nitrocellulose-coated glass slide was 6.91 ± 0.06 μm·s^{-1} at 25°C, ~20% higher than on whole myosin, and showed a high temperature sensitivity. The effect of the substrates on the ability of frog HMM to propel actin filaments was tested by comparing V_F obtained on nitrocellulose, trimethylchlorosilane (TMCS) and poly(methylmethacrylate) (PMMA). The highest value of V_F was obtained on TMCS (V_F ~20% higher than on nitrocellulose). Mechanical measurements with HMM fragments have been done in a simplified version of MYOMAC, where the motor proteins are randomly adsorbed on the flat tip of an etched optical fibre (diameter ~5 μm) the position of which is controlled by a piezoelectric actuator with nanometer precison. The HMM array is brought to interact with an actin filament attached to a bead trapped by the DLOT and then the HMM coated tip is pulled away from the filament. Statistical

analysis of the unbinding events shows that the rupture force of a single actin-HMM complex is ~13 pN.

Chapter 1 – INTRODUCTION

1.1 Rationale

1.1.1 The function of the molecular motor myosin II in muscle

The motor protein myosin II produces force and shortening in muscle during cyclic ATP-driven interactions with the actin filament. In each actin-myosin interaction, depending on the mechanical conditions, the myosin motor can generate a force of several pN or a displacement of the actin filament of several nm, as the myosin head (the myosin subfragment 1, S1, which contains the actin binding site and the catalytic site) undergoes a structural change (the working stroke, *d*). In the thick filament of each sarcomere, the structural unit of striated muscle, myosin II molecules are polymerized in two bipolar arrays, and in each array the motors work in parallel pulling the actin filament toward the centre of the sarcomere (Huxley & Niedergerke, 1954; Huxley & Hanson, 1954; Huxley, 1969).

When the external load is smaller than the isometric force generated by the array of motors, the actin filament slides past the myosin filament and the sarcomere shortens. In this case the myosin motors work as a collective motor, converting metabolic energy into mechanical work during cycles of actin attachment/detachment of individual motor domains. Reducing the load, the velocity of shortening increases, accompanied by the increase in the rates of energy (heat + work) liberation and ATP hydrolysis (Fenn, 1924; Hill, 1938; Huxley, 1957; Kushmerick *et al.*, 1969). The muscle develops the maximum power output when it shortens under a load ~1/2 the isometric force, at which the macroscopic efficiency is ~45% (Woledge *et al.*, 1985; Barclay *et al.*, 1993).

When an external load larger than the array force is applied to the active muscle, the motor array acts as a brake, very efficiently resisting the load with reduced metabolic cost. These properties are generated by the combination of structure-function of myosin II molecule with the array-type arrangement of the molecules, mechanically coupled by their connections to the myosin filament.

1.1.2 *In situ* and *in vitro* studies of myosin II

The array arrangement of the myosin II plays a critical role in determining the high power output and the high efficiency of the sarcomere. For this reason the mechanical and energetic properties of the myosin II as a collective motor can be described only *in situ*, in the muscle fibre, where the contractile proteins act in the preserved filament lattice. The motor function *in situ* is studied with the best temporal and spatial resolution by applying sarcomere level mechanical methods to single fibres isolated from frog muscle (Brunello et al., 2007; Piazzesi et al., 2007). In intact fibres, however, it is not possible to control the composition of the biochemical milieu of the myofilaments and relate the mechanical steps to the chemical transitions of the actomyosin cycle that leads to the transduction of the free energy of ATP hydrolysis into work. The preparation of election for studies of the chemomechanical coupling is the demembranated fibre from mammalian muscle (Hellam & Podolsky, 1969; Goldman et al., 1982; Caremani et al., 2008), but in this preparation the sarcomeric order is progressively lost in subsequent activations.

The *in vitro* motility assay (IVMA) is the technique for studying the molecular motors developed in the mid 80's (Sheetz & Spudich, 1983; Yanagida et al., 1984; Kron & Spudich, 1986; Ishijima et al., 1991; Finer et al., 1995) (Fig. 1.1). In this assay motor proteins (myosin, kinesin, etc) are randomly dispersed on the functionalized surface of a coverslip and promote the sliding of the respective filamentous track (actin filaments or microtubules). The motility produced by an ensemble of myosins is evaluated by measuring the velocity of sliding of the actin filaments (V_F), made fluorescent by labelling with rhodamine-phalloidin. V_F, that

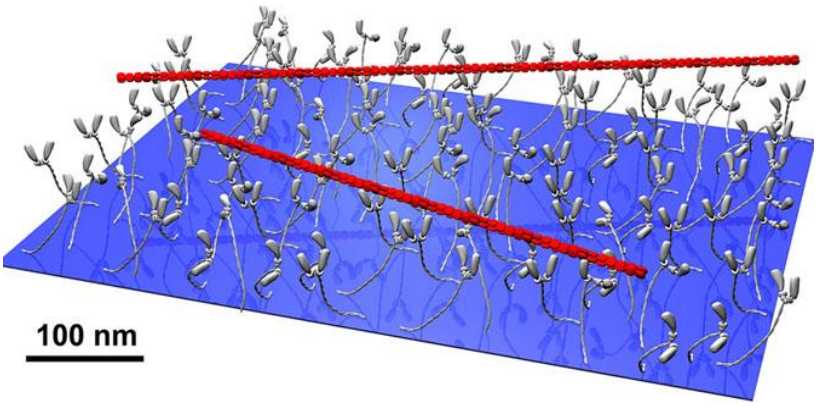

Fig. 1.1. Schematic representation of the *in vitro* motility assay (IVMA). The actin filaments (red) slide on the functionalized coverslip surface covered with myosin molecules (grey).

should correspond to the unloaded shortening velocity in the fibres (V_0) since axial movement of actin does not imply significant viscous drag, is a fundamental mechanical parameter to define the coupling between the biochemical and mechanical steps of actin-myosin interaction. Even if the sarcomeric arrangement of motors is lost, the IVMA offers the following advantages with respect to the *in situ* approaches: (*i*) the method allows direct control of the protein composition of the motility system, thus the function of the motor proteins can be defined in the absence of the effects of cytoskeletal structures and regulatory proteins; (*ii*) the use of purified proteins allows direct comparison of the motor mechanism of myosin II from skeletal muscle with that of other motors (like myosin V and kinesin); (*iii*) genetically modified proteins or mutant proteins can be easily examined. Major limits of the IVMA are that the motor ensemble is arranged at random and that the only mechanical output of the motors is the velocity at which actin is propelled in the absence of load.

The limits mentioned above could be overcome if we could measure the mechanical properties of myosin II in an isolated sarcomere, or, alternatively, in a sarcomere-like synthetic machine as that proposed in the following paragraph.

1.1.3 The project of a Myosin Based Machine (MYOMAC)

MYOMAC is a synthetic sarcomere machine that consists of a single actin filament interacting with a linear array of motor proteins myosin II regularly disposed on a nanostructured surface (Fig. 1.2). Under these conditions, when the actin filament is brought to interact with the motor array, the ensemble of myosin motors provides the condition for cyclic interactions with the actin filament, developing steady force and shortening. The experiments will be carried out in an flow cell that allows the biochemical composition of the solution to be rapidly changed. The mechanical outputs (force and shortening) will be measured by means of a double laser optical tweezers apparatus (DLOT) able to control either the length or the load with an adequate dynamic range (0.5-200 pN force and 1-10,000 nm shortening) and frequency response (force and length changes with ~2ms rise time).

The nanostructured support for the myosin motors allows to control the geometry of the myosin array in a way similar to the half-sarcomere, opening the possibility to study the effect of the steric organization of the motors on the mechanical and energetic properties of the motor array. MYOMAC, with respect to the skinned fibre preparation, allows the coupling between the biochemical and mechanical step of the actomyosin cycle to be investigated at picomolar and nanoscale level by the rapid control of the biochemical composition of the solution. The new assay finds application in different fields of research: in muscle biophysics and physiology it will allow understanding how functional diversity of muscle types depends on different myosin isoforms and the molecular and supramolecular mechanisms of maximization of power and efficiency; in muscle pathology it will allow investigation of the molecular basis of genetic diseases and therapies mostly related to regulatory and cytoskeletal proteins.

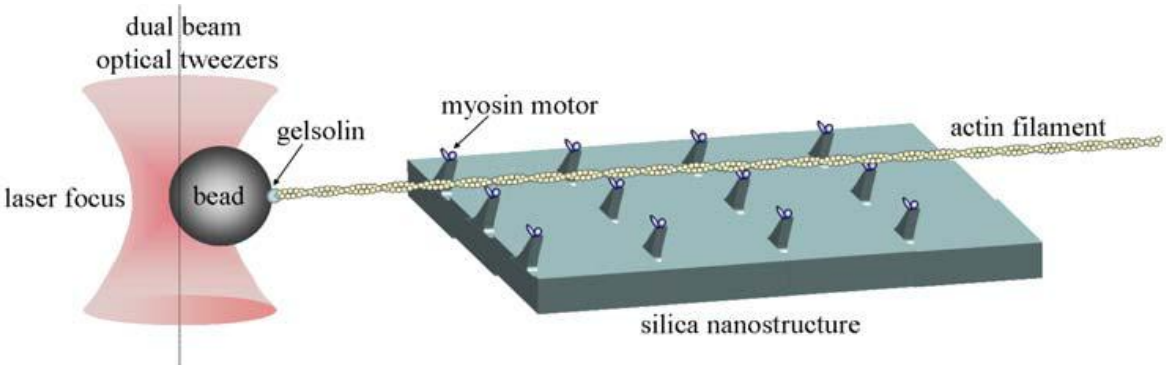

Fig. 1.2. Schematic representation of the MYOMAC experiment. The actin-attached bead is captured in the focus of the DLOT, the array of myosin motors is defined by the pattern of the edges on a micro-fabricated silica/quartz structure carried by the piezoelectric nano-positioner. Dimensions: bead diameter 1.5 μm, actin filament length 10 μm, distance between the myosin motors in each array ~100 nm.

1.1.4 Aim of the thesis

A motility system like MYOMAC allows any kind of molecular motors (non processive and processive motors, native and engineered proteins) to be tested. At this stage, there is a compelling reason to use, as motor protein, the myosin from frog skeletal muscle. In fact, the most reliable reference values for mechanical, kinetic and energetic parameters of sarcomeric myosins are provided by studies on intact fibres from frog skeletal muscle (Woledge *et al.*, 1985). The protocols for the extraction and purification of fully functional myosin II molecules from frog skeletal muscles have been recently developed in the Laboratory of

physiology of the University of Florence (Elangovan *et al.*, 2012). The myosin molecules prepared with these protocols preserve their enzymatic activity and have a long lasting IVMA activity. However preliminary tests revealed that whole myosin II molecule is not suitable for developing the nanostructured array of motors. In fact, it has been observed that when a solution, with the myosin molecules at the physiological ionic strength, is introduced into the experimental chamber, the proteins tend to aggregate and bind to any surfaces, also included the stem carrying the nanostructured surface. This problem was solved using the proteolytic fragments Heavy Mero Myosin (HMM) of the whole myosin II molecule, or its sub-fragment S1, which do not self-aggregate at the physiological ionic strength, as they are deprived of the LMM portion responsible for the polymerization of the molecules into filaments. HMM is still a dimeric motor, while S1 is monomeric. These features will reveal particularly useful in future experiments on MYOMAC aimed at investigating the physiological role of the dymeric nature of the motor protein.

The aims of this thesis are: (*i*) the development of the protocols of purification of frog myosin II fragments HMM and S1 with long last viability to be used in myosin-based machine devices; (*ii*) kinetic and mechanical characterization of the myosin II fragments using both transient kinetic experiments and IVMA; (*iii*) test for selection of the best coating for attachment of the myosin motors to the nanostructure; (*iv*) mechanical measurements on a simplified version of the MYOMAC consisting of a few myosin motors randomly dispersed on the flat tip of an etched optical fibre.

1.2 Background

1.2.1 Structure of the skeletal muscle

The skeletal muscle is the basis of the movement and locomotion of all vertebrates. The muscle is made of a large number of elongated cylindrical cells (the muscle fibres), spanning the length of the muscle and attached to the bones

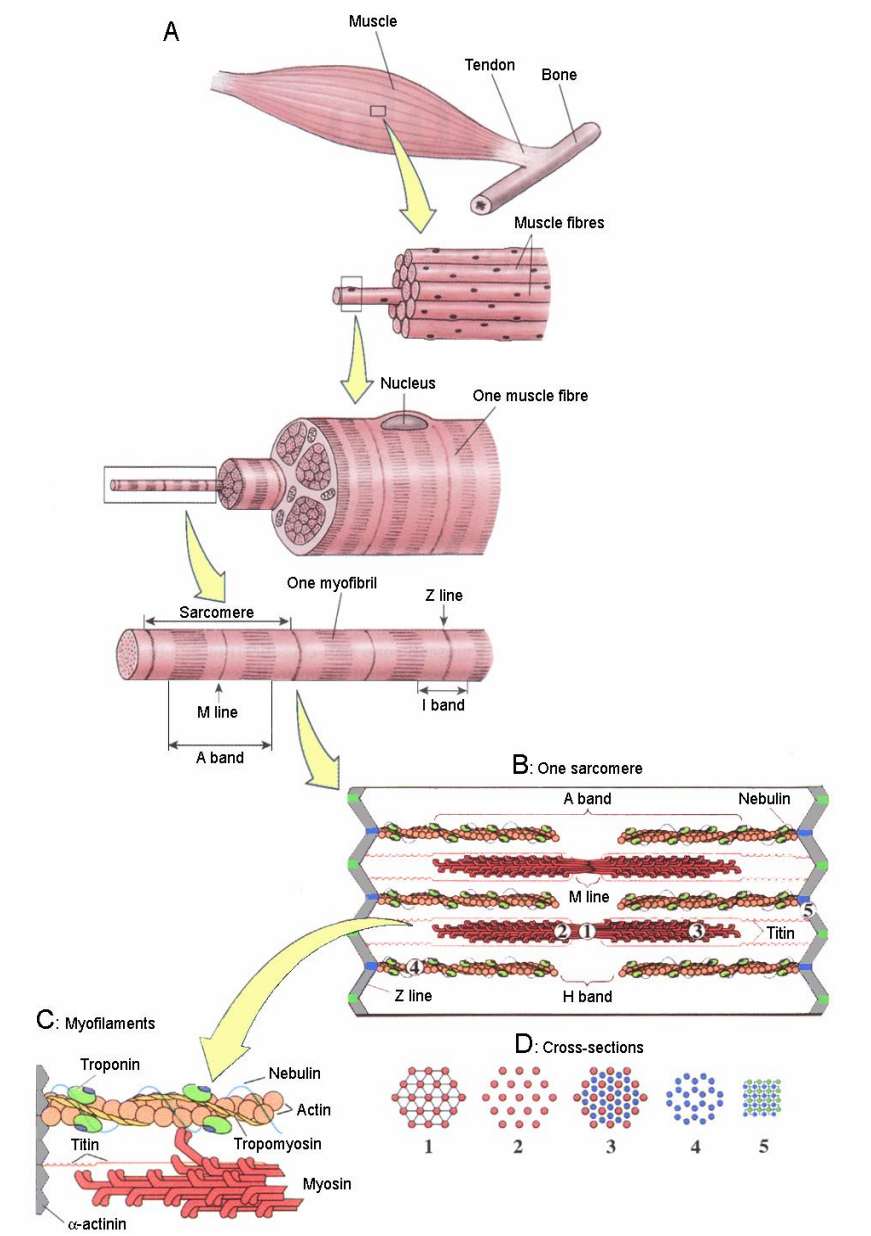

Fig. 1.3. Different level of organization of the skeletal muscle. **A.** Skeletal muscle in living frog, from the tissue to a single cell or fibre, and from the single fibre to the myofibril. **B.** The sarcomere, the structural unit of striated muscle. **C.** Thick (red) and thin (orange) filaments with regulatory (troponin and tropomyosin) and structural (nebulin, titin and α-actinin) proteins. **D.** Arrangement of thick and thin filaments in the cross-section of the sarcomere at different positions along it.

via the tendons (Fig. 1.3). These cells are multinucleated with diameter ranging from 20 to 200 µm and are cross-striated with a periodicity of about 2.0 µm (at the slack length). Most of the intracellular space within the fibre is occupied by myofibrils, cylindrical structures of 1-2 µm in diameter, that run along the length of the muscle fibre and contain the contractile proteins, actin and myosin, arranged in thin (actin) and thick (myosin) filaments that are in register across different myofibrils and provide the striated appearance to the muscle fibre.

1.2.2 Structure of the sarcomere

From a structural point of view the skeletal muscle is classified as striated muscle. In fact, under the light microscope, the skeletal muscle appears striated due to the regular repeat of dark bands (A bands) and light bands (I bands). Electron microscopy (Fig. 1.4) reveals that the striations are due to the regular repeat of two sets of filaments: the thick filaments (1.6 µm long, 12 nm in diameter) due to polymerization of the myosin molecules and the thin filaments (1 µm long, 8 nm in diameter) due to polymerization of actin molecules. The thin filaments extend from the Z disk, at the centre of the I band, and partially interdigitate with the thick filaments in the A band. The centre of the A band is bisected by a dark M line, containing proteins that link the thick filaments together in the cross-section of the myofibril. The zone in the A band, where there is no overlap with thin filaments is called H band. The portion between two consecutive Z lines defines the structural unit of the striated muscle, called

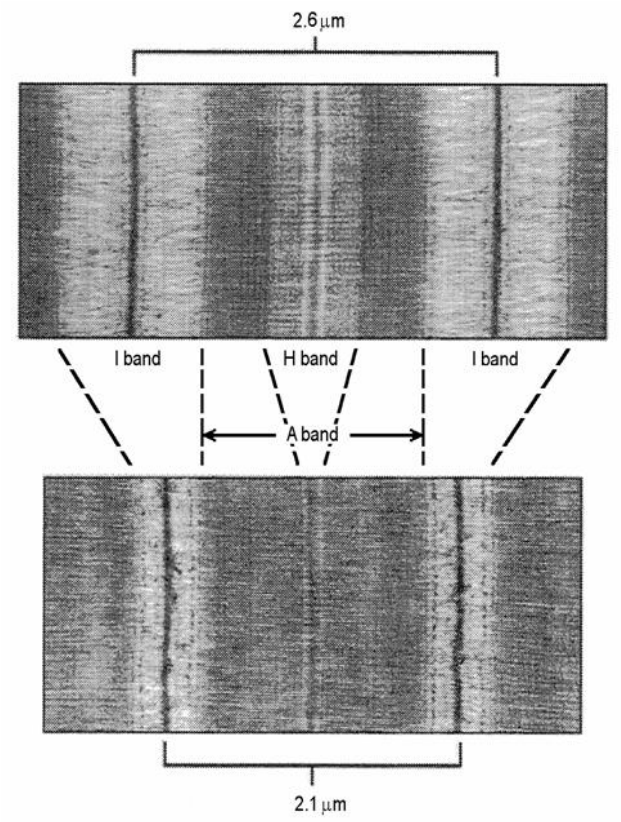

Fig. 1.4. Electron microscopy images of the sarcomere showing the arrangement of thick and thin filaments producing the striated appearance of muscle. **Upper panel.** Sarcomere length 2.6 µm. **Lower panel.** Sarcomere length 2.1 µm. Sarcomere shortening is the result of thin filaments sliding into thick filaments, as indicated by the reduction of the widths of I and H bands while the width of A band remains constant.

sarcomere that repeats along the whole fibre. Muscle shortening occurs by reciprocal sliding of the thick over the thin filaments (Huxley & Niedergerke, 1954; Huxley & Hanson, 1954).

As seen in the cross-section of a myofibril, thick and thin filaments are arranged in a double hexagonal lattice in the overlap zone (Fig. 1.3, 3). Each thick filament is surrounded by 6 thin filaments, while each thin filament is surrounded by 3 thick filaments, thus the ratio of the thick filaments over thin filaments is 1:2. A different symmetry is visible from the cross-section at the level of the Z line, where thin filaments and other cytoskeletal proteins are arranged in a tetragonal pattern (Fig. 1.3D, 5): each thin filament from a sarcomere is connected, across the Z line, to 4 thin filaments from the next sarcomere.

1.2.3 Structure of the thin filament

The thin filaments are made by the polymerization of the globular protein actin (G-actin, 42 kDa) and the regulatory proteins troponin and tropomyosin. In the presence of ATP the actin monomers polymerize spontaneously to form the backbone of the thin filament, F-actin, that has a double helical symmetry. Troponin is a complex made of three subunits: troponin C (TnC), troponin T (TnT) and troponin I (TnI). The elongated tropomyosin dimers are associated to form a helical filament that lies in the major groove of the actin filament. Each tropomyosin dimer spans seven actin monomers and the troponin complex is also associated to actin every seven repeats (Fig. 1.5A).

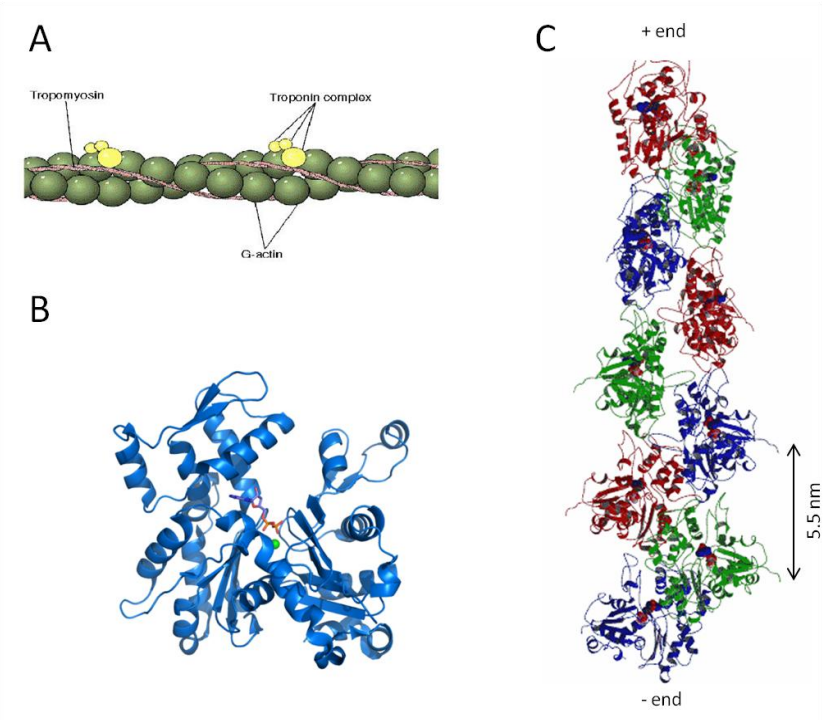

Fig. 1.5. The thin filament. **A.** Thin filament structure, relative positions of troponin and tropomyosin on the backbone of the double helix of F-actin; **B.** Crystallographic model of G-Actin (blue), with bound ATP (red) and Mg2+ (green); **C.** High resolution structure of F-actin made by 9 G-actin monomers, each coloured differently. F-actin is a polarised structure and the distance between subsequent binding sites for myosin in the same strand of the double helix is about 5.5 nm.

The crystallographic model of the G-actin (Kabsch *et al.*, 1990) shows that it consists of two similar domains each of which contains a 5-stranded β-sheet and associated α-helices and has a binding pocket for ATP and Mg^{2+} (Fig. 1.5B). The high resolution model of F-actin is then derived from the structure of G-actin and the X-ray diffraction patterns of oriented actin filament gels (Holmes *et al.*, 1990; Holmes *et al.*, 1993). The model consists of 9 actin molecules arranged in 6 left-handed turns repeating every 36 nm (Fig. 1.5C). The actin monomers are asymmetrical, so that the ends of F-actin are structurally and functionally different. The polymerization of the filaments occurs only with addition of G-actin at the barbed end (the + end), that in the sarcomere is connected to the Z line) and the actin filament slides on myosin molecules only toward the free end (the - end), that in the sarcomere points toward the M line. The binding sites for myosin in each strand of the double helical F-actin are spaced 5.5 nm apart.

1.2.4 Structure of the thick filament and the myosin molecule

The thick filament is made by the myosin molecules polymerized so as to produce two bipolar arrays of motors that pull the two actin filaments from the two halves of the sarcomere toward the centre. There are about 150 myosin molecules per half-thick filament. The globular part of the myosin molecule, the myosin head, projects from the thick filament in crowns of three couple of heads at an angle of 120°. Subsequent crowns emerge with axial periodicity of 14.3 nm and are rotated by 40° so that their helical periodicity is 42.9 nm (Fig. 1.6A). As a consequence of the antiparallel arrangement of the molecules in the two halves of the thick filament, a region of ca 160 nm in the centre of the filament, formed by the tail of the myosin molecules, called the bare zone, is free of heads. The thick filament contains structural proteins such as protein C and titin. These proteins have been shown to play an important role in the organization of the thick filament structure (Seiler *et al.*, 1996) and in the conservation of filament alignment.

The myosin molecule is a dimer with molecular weight (MW) ~520 kDa, consisting of two heavy chains (MW 220 kDa), each composed of a 150 nm ‘tail’ and a globular ‘head’ at one end, and two pairs of light chains (each light chain with MW 20 kDa) (Fig. 1.6B, a). Each heavy chain can be enzymatically separated in different fragments depending on the enzyme used for the digestion and the solution composition (Fig. 1.6B, b): (*i*) in the absence of Mg^{2+}, digestion by trypsin

results in two fragments, the Light MeroMyosin (LMM) that forms most of the tail, and the Heavy MeroMyosin (HMM), with two elongated globular head regions; (*ii*) digestion with trypsin in the presence of Mg^{2+} results in three fragments, the two globular S1 portions or heads, a rod-like S2 portion, the short part of the tail, proximal to the head, emerging from the thick filament, and the LMM, the long part of the tail lying in the filament backbone. In this conditions the enzyme cuts the heavy chain molecule just above the regulatory light chain binding site, towards the N-terminal end of the molecule, so that the S1 portion loses the regulatory light chain (see Fig 2.1 in Materials and Methods section); (*iii*) digestion with papain results in the same fragments as trypsin digestion in the presence of Mg^{2+}, but in this case the enzymatic cut occurs before the light chain binding site and the S1 fragments retain the whole light chain. The LMM, the myosin tail, is a coiled-coil α-helical structure, about 2 nm in diameter and 150 nm long, while the heads are about 15 nm long and up to 5 nm wide. Myosin rods have self assembly properties, that is, they bind to each other to polymerize in low salt solution.

The crystallographic structure of the myosin has been determined only for the S1 fragment, comprising the first 843 residues, in the absence of ATP (Fig.

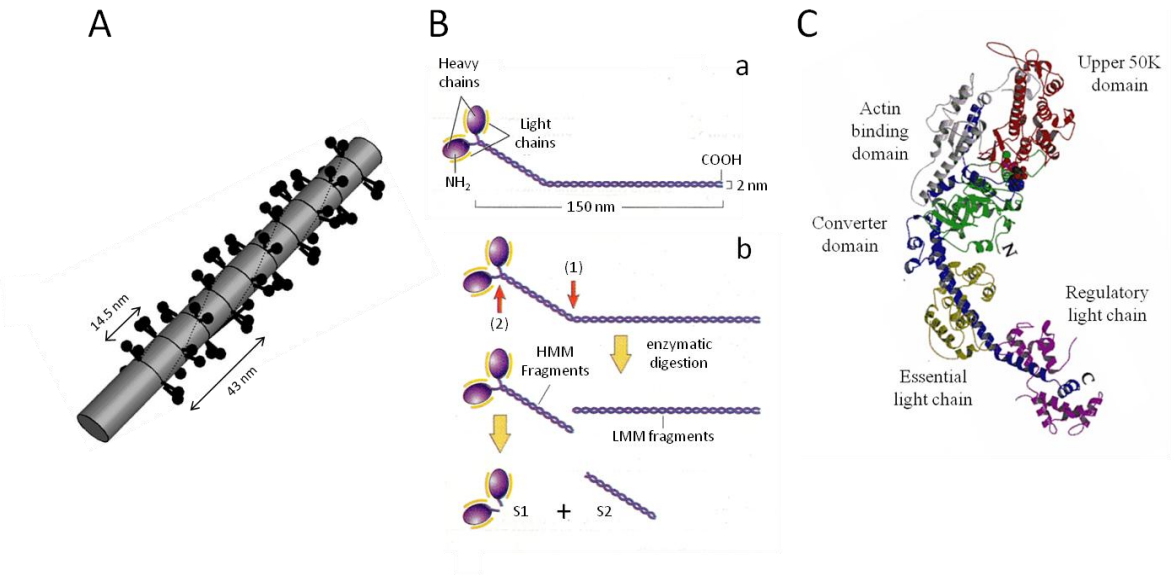

Fig. 1.6. The thick filament and the molecular motor myosin II. **A.** Schematic representation of the myosin molecule disposition on the thick filament in vertebrate skeletal muscle. The myosin heads project from the thick filament in crowns of three couples of heads every 14.5 nm with an angle of 120°; **B. a)** Schematic representation of myosin II motor. The molecule is a dimer composed of a couple of heavy chains and two couples, one for each heavy chain, of light chains; **b)** The heavy chains can be split by proteolytic enzymes. The numbers (1) and (2) indicate the proteolytic site of trypsin and papain respectively; **C.** Crystallographic model of the S1 fragment. The N-terminal region of the molecule contains both the ATP hydrolysis site and the actin binding site. The C-terminal acts as a lever arm and contains the binding site of the light chains.

1.6C) (Rayment *et al.*, 1993b). The S1 portion that includes both the site of attachment to actin and the site for ATP hydrolysis, has an elongated head, containing a 7-stranded β-sheet and associated α-helices. The long α-helix that constitutes the C-terminal region of the head, the so called “lever arm”, provides the connection to the S2 portion attached to the thick filament. Using the electron density maps of actin filaments decorated with myosin heads, it is possible to fit together the crystallographic structures of actin and myosin S1 and recover the relative orientation of the myosin head and the actin filament (Rayment *et al.*, 1993a). The comparison of the ATP-free S1 structure with the structure obtained with ATP analogues (as $ADPAlF^{-4}$) in the catalytic site produced a model for the working stroke consisting in an interdomain structural change that implies rotation of the lever arm about a pivot on the catalytic domain that is firmly attached to actin. The length of the lever arm amplifies, to up to 11 nm, the axial movement at the level of the head-rod junction The interaction of myosin with actin is the trigger for the working stroke. The interaction starts with a weak electrostatic interaction that is followed by a stronger hydrophobic interaction and further ionic interactions. Thus the first complex formation has a marked dependence on ionic strength and is probably driven by long range ionic interactions.

1.2.5 The actin-myosin ATPase cycle

The free energy required for the execution of the working stroke is provided by the hydrolysis of a molecule of ATP in the catalytic site of the S1 portion of the myosin molecule. The products of ATP hydrolysis are adenosine diphosphate (ADP) and inorganic phosphate (Pi). The acto-myosin ATPase cycle can be described as a series of precisely coupled mechanical, structural and biochemical events for the conversion of chemical energy into movement (Fig. 1.7). The steps of ATP hydrolysis cycle of the acto-myosin complex have been defined with protein solution studies by Lymn & Taylor in 1971 using a rapid-mixing apparatus. In these studies the key concepts of the biochemical mechanism of the crossbridge cycle are defined: (*i*) the reduction of myosin affinity to actin by ATP binding; (*ii*) the reduction of the affinity between myosin and ATP hydrolysis products by actin binding. In particular even if myosin is able to rapidly hydrolyse an ATP molecule in the absence of actin, the hydrolysis products are rapidly released only if actin binds to myosin (Fig. 1.7 step 4-6). The acto-myosin complex

after the hydrolysis product release, has a high affinity for ATP and the ATP binding induces the fast irreversible dissociation of the complex (step 1) followed by the rapid hydrolysis by myosin of ATP into ADP and Pi which both remain tightly bound to the myosin head (step 2). The cycle restarts because myosin with the hydrolysis products tends to bind (step 3). As indicated by calorimetric studies of the enthalpy changes associated to the various steps of the cycle, most of the free energy is released in correspondence of Pi release (White & Taylor, 1976). This finding suggests that the biochemical step coupled with the working stroke is Pi release (Fig. 1.7A step 4 and 5). The kinetics of the ADP release step is strain dependent in muscle myosin (Nyitrai & Geeves, 2004; Geeves & Holmes, 2005) so that this step becomes the rate limiting step during muscle contraction at high load and explains how the reduction of load on the contracting muscle increases both ATPase rate and energy liberation. The structural changes of the myosin associated with the biochemical steps are schematically represented in Fig. 1.7A.

According to crystallographic model (Rayment *et al.*, 1993a) the working stroke in the myosin head consists in the tilting of the lever arm, constituted by the light chain domain, about a fulcrum in the catalytic domain. As demonstrated by

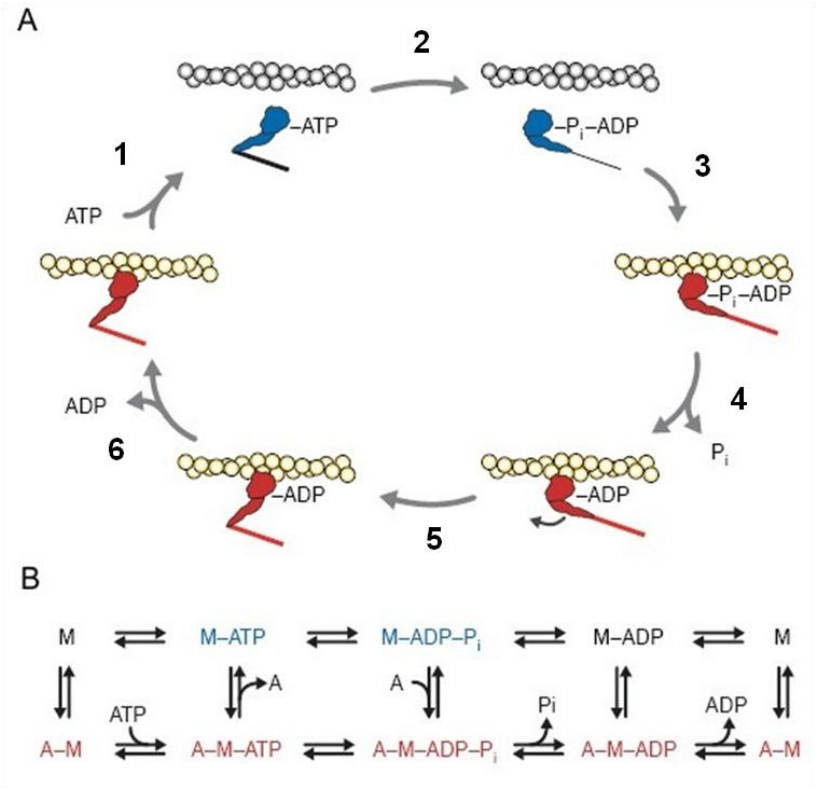

Fig. 1.7. The actin-myosin ATPase cycle. **A.** Schematic diagram showing the different states of the cross-bridges during the ATPase cycle. Actin-bound states are in red, detached states are in blue. **B.** Chemical states of the ATPase cycle: In the upper line myosin (M) binds ATP, hydrolyses it to ADP-Pi and releases the products in the absence of actin, but phosphate release is very slow. In the lower line binding of actin (A) accelerates phosphate release, which is associated to the working stroke. ADP release is the slowest step of the bound states. Rebinding of ATP causes dissociation from actin and starts the cycle again.

the increase of the intrinsic fluorescence of tryptophan residues, the myosin head recovers the initial state (pre-working stroke) during step 2, when it is detached from actin and hydrolyses an ATP molecule.

1.2.6 Actin-Binding Proteins

Actin is an essential component of the cytoskeleton of eukaryotic cells. Indeed, actin filaments are involved not only in the contraction of muscle cells but also in the generation and maintenance of cell morphology and polarity, in endocytosis, intracellular trafficking, cell motility and division. In the cytoplasm, the assembly and disassembly of actin filaments, and also their organization into functional higher-order networks, are regulated by a lot of actin-binding proteins (ABPs) (Dos Remedios *et al.*, 2003). Classification of these ABPs can be reduced to seven groups on the basis on their specific activity. (*i*) Monomer-binding proteins sequester G-actin and prevent its polymerization (e.g., thymosin β4); (*ii*) F-actin-depolymerizing proteins (e.g., CapZ and profiling); (*iii*) Filament end-binding proteins cap the ends of the actin filament preventing the exchange of monomers at the pointed end (e.g., tropomodulin) and at the barbed end (CapZ); (*iv*) Filament severing proteins shorten the average length of the actin filaments by binding sideways along F-actin and cutting it into two pieces (e.g., gelsolin); (*v*) Cross-linking proteins contain at least two actin binding sites and promote the formation of filament bundles, branching filaments and three dimensional F-actin networks (e.g., Arp2/3); (*vi*) Stabilizing proteins bind sideways along an actin filament and prevent depolymerization (e.g., tropomyosin); (*vii*) Motor proteins use F actin as a track to generate movement (e.g., the myosin family of motors).

Some of these proteins belong to more than one group, for example gelsolin is capable of severing the actin filaments and capping its barbed end (Gremm & Wegner, 2000) and the Arp2/3 complex can nucleate filament formation, elongate filaments and establish branch points in actin networks.

1.2.6.1 Gelsolin

Gelsolin is an ubiquitous Ca^{2+} activated protein with the property of severing and capping actin filament in eukaryotic cells. It has been implicated in the regulation of cell motility, in the transduction of signals into dynamic rearrangement of the cytoskeletal architecture, and even in the stimulation of

programmed cell death in certain vertebrate cells (Kwiatkowski *et al.*, 1989; Kothakota *et al.*, 1997).

In the presence of calcium, gelsolin severs actin filaments and caps their barbed end, thereby preventing monomer addition to their fast-growing ends. The gelsolin-capped barbed ends are highly stable and allow the disassembly of populations of actin filaments by subunit loss from pointed end (Pantaloni & Carlier, 1993; Perelroizen *et al.*, 1996). Gelsolin activity is controlled by several elements: gelsolin is sequestered by phosphatidylinositol 4,5-bisphosphate (PIP_2) at cell membrane (Janmey *et al.*, 1987) and held in an inactive state; hydrolysis of PIP_2 releases gelsolin into the cytoplasm; calcium activates free gelsolin allowing it to cap and sever actin filaments and selected filaments are uncapped by PIP_2-rich membrane allowing actin polymerization to proceed (Janmey & Stossel, 1987; Allen, 2003).

Gelsolin is a 80 kDa protein composed of six compact domains (100-125 amino acid residues), termed G1-6 (Kwiatkowski *et al.*, 1986), that are connected by linker regions of varying lengths (Fig. 1.8) Studies of proteolytic fragments of gelsolin (Kwiatkowski *et al.*, 1985; Chaponnier *et al.*, 1986; Hwo & Bryan, 1986) and subsequent investigations of recombinants of individual segments (Way *et al.*, 1989; Pope *et al.*, 1991) identified three actin binding regions with different actin binding properties and calcium dependence: a calcium independent strong monomer binding fragment (G1), a calcium independent filament binding fragment (G2-3), and a calcium dependent monomer binding fragment (G4-6).

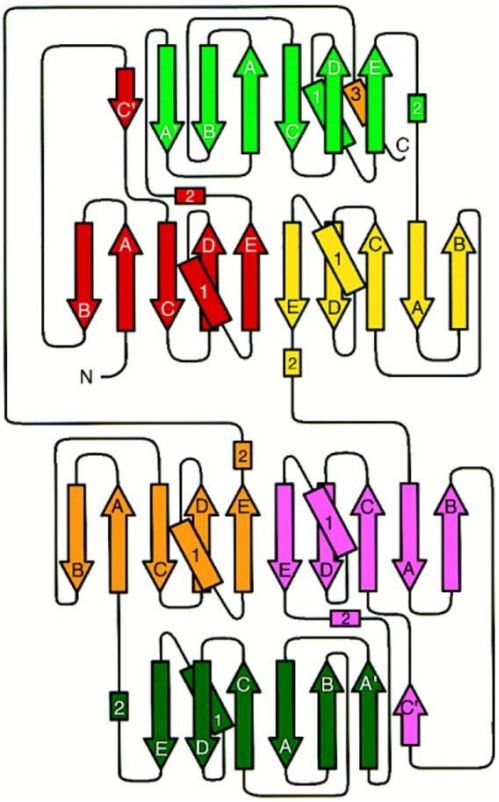

Fig. 1.8. Schematic representation of the topology of the six domains of gelsolin protein. β sheets are depicted by arrows and α helices as rectangles.

Protein crystallography has identified a Ca^{2+} binding site in each gelsolin domain. The type 2 Ca^{2+}-binding sites are responsible for the structural

change that activates gelsolin. Type 1 sites, with lower calcium affinity, are located at the interface between actin:G1 and actin:G4 and likely modulate the affinity of activated gelsolin for actin (Choe *et al.*, 2002).

There is still a debate concerning the number of actin filament subunits that are involved in actin-gelsolin interaction and to which actin subunit in the filament the G4-6 fragment is bound.

1.2.7 Bead Tailed Actin (BTA)

Actin filaments have a well-defined polarity (section 1.2.3). Based on arrowhead pattern created by decoration of actin filament with myosin, one end of the filament is called barbed end (+) and the other pointed end (-). The two ends are functionally different as regards motor protein movement and force generation (see section 1.2.3) and for this reason it is necessary to control the polarity of the actin filament in *in vitro* experiments.

As outlined in the previous section, gelsolin protein is capable of severing and capping the barbed end of actin filaments. These gelsolin properties have been exploited to attach the proper end (the barbed end) of an actin filament to the polystyrene bead trapped by the laser (Suzuki *et al.*, 1996). The bead-gelsolin-actin filament complex slids smoothly in IVMA experiments trailing the bead at its end (this is why it has been called bead-tailed actin filaments (BTA)). Using this preparation it has been possible to estimate the torque and axial rotation generated by the sliding force in IVMA (Suzuki *et al.*, 1996; Sase *et al.*, 1997) and measure, with the optical tweezers, the unbinding force and the load dependence of the lifetime of the actomyosin rigor bond (Nishizaka *et al.*, 1995; Nishizaka *et al.*, 2000).

The BTAs have been also used to measure the rupture force of ABPs-Actin filament interaction *in vitro* (Miyata *et al.*, 1996; Ferrer *et al.*, 2008) showing that an actin filament attached to a bead by gelsolin protein can bear force up to 150 pN.

In this thesis, the BTA preparation is used to set the correct polarity of the actin filament interacting with the myosin array in the simplified version of MYOMAC.

1.2.8 *In vitro* studies of motor proteins

Motor proteins have been studied using a wide range of different approaches that can be grouped in: (*i*) *in solution* techniques (e.g. biochemical transient kinetics) that allow direct measurements of several kinetic parameters of the ATPase cycle of motor proteins; (*ii*) *in vitro* assays (e.g. *In vitro* motility assay, optical tweezers methods, etc.) where the motor proteins are studied at single molecule level; (*iii*) *in situ* techniques (e.g. intact and skinned single fibres mechanics) that allow studying motor proteins in their native arrangement.

The *in vitro* assays, differently to the others approaches, enable rapid detailed control of the biochemical environment, the use of protein engineering and single molecule mechanical measurements. A key limitation of the *in vitro* techniques is the loss of the *in vivo* ordered arrangement of the motor proteins with potential disturbances of the mechanics of motor function (Tanaka *et al.*, 1998).

In this thesis two, among the most commonly used *in vitro* techniques, *in vitro* motility assay and optical tweezers, are used to study the kinetics and mechanics of myosin motors from frog skeletal muscle. Below an overview and a detailed description of this two techniques is presented.

1.2.8.1 *In vitro* motility assays (IVMAs)

The *In vitro* Motility Assays (IVMAs) are among the most powerful techniques to study the motility systems considering the relative simplicity of their realization and the possibility to apply these techniques to a wide range of different motility systems in different conditions. In these assays the motility of purified motor proteins along purified cytoskeletal filaments is reconstituted in cell-free condition. The IVMAs are performed in two major configurations. In the first version, motor-coated beads are observed as they move along oriented arrays of actin filaments or microtubules that are immobilized on a surface (the bead assay, Fig. 1.9 A) (Sheetz & Spudich, 1983; Spudich *et al.*, 1985). In the second and most common version (the gliding motility assay, Fig. 1.9 B) (Kron & Spudich, 1986; Kron *et al.*, 1991), fluorescent cytoskeletal filaments are observed as they are transported by randomly oriented immobilized motors. In this assay the length and sliding velocity (V_F) of the filaments and the fraction of motile filaments can been readily measured using a fluorescence microscope. In this thesis the gliding

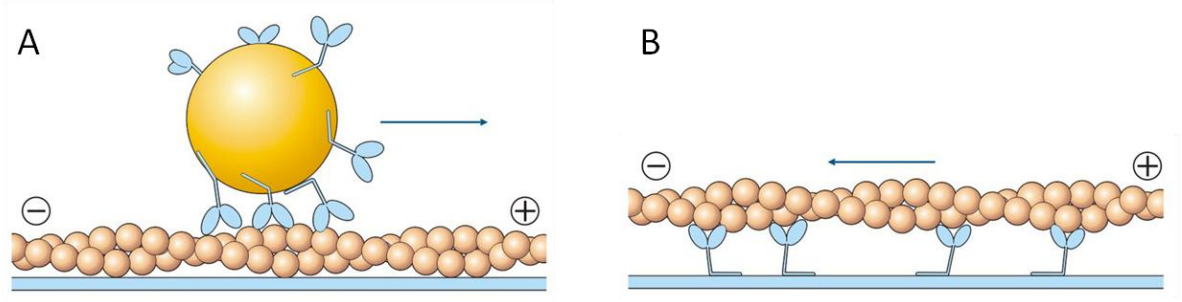

Fig. 1.9. *In vitro* motility assays. **A.** Bead assay. The cytoskeletal filaments are attached to the substrate and the bead moves under the action of the motor proteins adsorbed on its surface. **B.** Gliding assay. In this case the cytoskeletal filaments glide on the motor protein coated surface. In bead assay the action of the motors moves the bead toward the plus end of the filament, in the gliding assay the filament moves with the minus end leading.

motility assay is used to characterize frog myosin II activity and in the remainder of the text the term *in vitro* motility assay or IVMA will be used to refer to this configuration.

In 1987, Toyoshima *et al*. showed that the S1 portion of the muscle myosin II is sufficient to move actin filaments *in vitro* demonstrating that (*i*) no portion of the myosin rod is required for movement generation; (*ii*) the motor portion of the molecule is located in the myosin head. The IVMA experiments have also demonstrated that the direction of movement is determined by the actin filament polarity and not by the orientation of motor proteins (Toyoshima *et al.*, 1989), suggesting also that myosin molecules have a great flexibility that allows reorienting of the molecules to sustain the movement. The direction of the movement is defined by filament polarity for any motility system, also using kinesin and microtubules as motor protein and track (Howard & Hyman, 1993). In all cases in the gliding assay the filamentous track moves with its minus end leading while in the bead assay the motor moves the bead toward the plus end.

One of the most important advantage of the IVMA approach with respect to *in situ* approach is the possibility to easily investigate the motility properties of engineered motor proteins. This advantage has provided many new insights into to the mechanism of force and movement generation by myosin molecule. A series of mutant of Dictyostelium myosin with shorter and longer neck region have been used in IVMA to test the swinging lever arm model (Uyeda *et al.*, 1996). As predicted by the model, it was found that the step size and consequently the actin sliding velocity, increases linearly with the neck length. Another mutant of Dictyostelium myosin containing an S456L substitution in the switch II region has

been used in *in vitro* motility assay to investigate the role of switch II loop of the myosin head in the chemo-mechanical coupling (Murphy *et al.*, 2001). The sliding velocity on the mutant was one tenth of that on wild type as a result of the longer time the myosin mutant spends in the strongly bound state and the shorter step size. In contrast, the ATPase rate remained unchanged. These findings indicate that the ATPase activity had been uncoupled from the mechanical activity and demonstrate the crucial role of switch in relating the nucleotide state to the conformational state of the myosin molecule.

The *in vitro* motility assay approach has given an important contribution to the study of the functional differences between different myosin isorfoms. In skeletal muscle, Myosin Heavy Chains and Myosin Light Chains exist in different isoforms that combine to give rise to a large number of myosin isoforms (Schiaffino & Reggiani, 1996). It is generally accepted that the mechanical properties of skeletal muscles, e.g. the unloaded shortening velocity, V_0, are to a large extent determined by the myosin isoform expressed in their fibres. Accordingly to this hypothesis, IVMA experiments have shown that different myosin isoforms translocate actin filaments at distinct velocity (Lowey *et al.*, 1993; Canepari *et al.*, 1999). Moreover, the hypothesis that ADP release step ($k_{\text{-ADP}}$) of the actomyosin ATPase cycle is the major determinant of the unloaded shortening velocity (V_0) of myosin isoforms (Siemankowski *et al.*, 1985; Weiss *et al.*, 2001; Capitanio *et al.*, 2006; Nyitrai *et al.*, 2006; Iorga *et al.*, 2007) has been confirmed using the IVMA approach. $k_{\text{-ADP}}$ was measured of pure slow and fast myosin isoforms (Canepari *et al.*, 2012) and of myosin II from frog skeletal muscle (Elangovan *et al.*, 2012). In all cases, the value of $k_{\text{-ADP}}$ was of the right magnitude for the ADP release step to be considered the process that determines V_0 *in situ*.

In the *in vitro* motility assay the motor proteins are adsorbed to artificial functionalized surfaces. Conventionally, nitrocellulose films are used as a substrate for protein adsorption, but different silanized surfaces, polymers and lipid bilayers have also been used (Bunk *et al.*, 2003; Sundberg *et al.*, 2003; Albet-Torres *et al.*, 2007; Albet-Torres *et al.*, 2010; Persson *et al.*, 2010). In 2003, Bunk *et al*. assessed five different resist polymers for HMM adsorption using IVMA. One group of resists (MRL-600.1XP and ZEP-520) exhibited high quality motility of actin filaments in terms of sliding velocity and fraction of motile filaments. However, for all resists, V_F was about 30% lower than nitrocellulose-functionalized

surfaces. A second group of resists (PMMA-200, PMMA-950 and MRI-9030) showed a low quality of motility with only few smoothly moving filaments. These differences in actin motility between the two groups of resists was exploited by the authors to confine the actin filament movement.

Silanes are a family of chemical compounds synthesized starting from silane through substitution of one or more hydrogen atoms with different chemical groups. Motor protein adsorption on surfaces derivatized with different silanes has been studied in IVMA, correlating the actin filament sliding velocity with the chemical and physical properties of the surfaces including contact angle, surface charge and RMS roughness (Sundberg *et al.*, 2003; Albet-Torres *et al.*, 2007; Persson *et al.*, 2010). The highest motility quality has been observed when HMM fragments were adsorbed on Trimethylchlorosilane (TMCS) coated surfaces (VF ~20% higher than nitrocellulose coated surfaces). Moreover it was reported that the capability of HMM to propel actin filaments is influenced by the contact angle of negatively charged HMM adsorbing surfaces. The degree of negative surface charge is negatively correlated with both contact angle and sliding velocity. These results are consistent with a model according to which the impaired function of HMM adsorbed to lower contact angle and higher negatively charged surfaces is

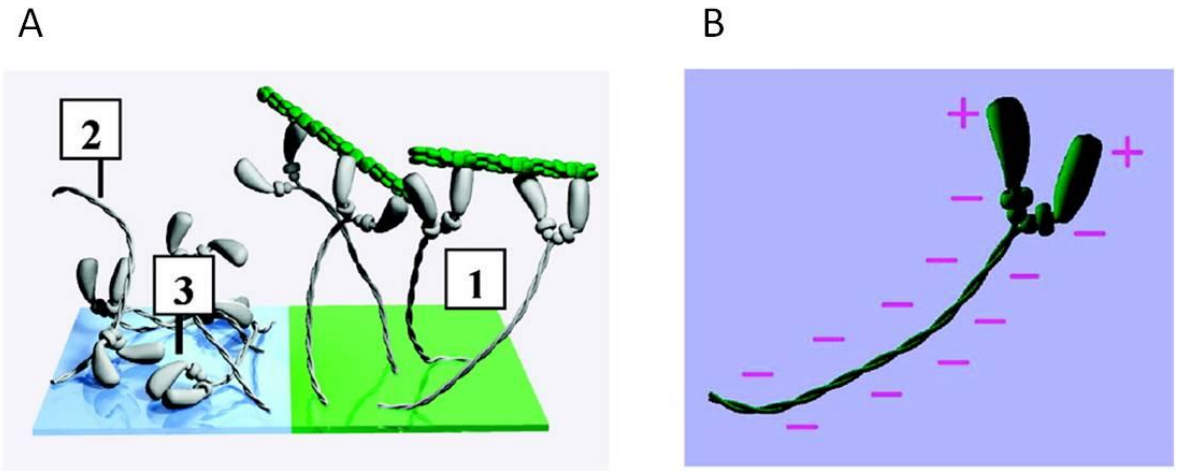

Fig. 1.10. Mode of motor proteins absorption on functionalized artificial surfaces. **A.** Model for HMM adsorption on strongly negatively charged surfaces (e.g. SiO_2) and low negative charged surfaces (e.g. TMCS-derivatized surface). On low negative charged surface, HMM is assumed to adsorb only via the C terminal end of the tail segment (configuration 1). For adsorption on strongly negatively charged surfaces, in addition to this configuration, the model provides two other configurations (2 and 3) that involve adsorption via the myosin head. Configurations 2 and 3 are believed to be possible mainly as a result of electrostatic interactions. As illustrated by the presence of short actin filaments, only configuration 1 is able to bind actin filaments. **B.** Schematic representation of the overall charge distribution on the myosin molecule surface. Note the negatively charged S2 domain, negatively charged light chain binding domain with light chains and the positively charged head domain (from (Albet-Torres *et al.*, 2007)).

attributed to different mode of HMM adsorption rather than to different HMM densities (Fig 1.10, (Mansson *et al.*, 2008)). Indeed, entropically driven adsorption of the C terminal, flexible, S2 domain would be likely on both the high and low contact angle surfaces (configuration1 in Fig. 1.10A). In contrast, electrically driven adsorption of the myosin head via positively charged regions, most notably the actin-binding site (Fig. 1.10B), would be more likely on low contact angle-high negatively charged surfaces (configuration 2 and 3 in Fig. 1.10A). This would result in myosin heads devoid of actin binding site and impaired actin propelling capabilities.

1.2.8.2 Single molecule mechanics: The optical tweezers

Force plays a fundamental role in all the motility systems. Force is generated in the cell during processes as diverse as chromosomal segregation, replication, transcription, translation, translocation of proteins across the membrane, cell locomotion, among others. The study of these processes has been revolutionized over the last 20 years by the development of single molecule manipulation techniques that permit measurement of force and displacement generated by single molecules ranging from cells to proteins. Single-molecule techniques allow following reactions at single molecule level and thus obviates problems associated with population averaging inherent in ensemble measurements. Rare or transient phenomena that are otherwise hidden by averaging can be resolved, provided that the measurement technique has the required resolution.

The most commonly employed single molecule techniques are force atomic microscopy (AFM) (Binnig *et al.*, 1986; Lee *et al.*, 1994), optical tweezers and micro needle manipulation (Kishino & Yanagida, 1988; Cluzel *et al.*, 1996; Essevaz-Roulet *et al.*, 1997). In optical tweezers experiments a micro sized particle as cells, bacteria, viruses and artificial beads, with an index of refraction higher than the surrounding medium is trapped by optical force in an electric field gradient near a laser focus (Ashkin & Dziedzic, 1987; Ashkin *et al.*, 1987; Smith *et al.*, 1996). Because the optical trap functions as a mechanical potential well and displays virtual spring properties, forces may be measured by following bead displacement from its equilibrium position in the trap centre. Optical tweezers are typically compliant (<1 $pN \cdot nm^{-1}$) and possess a force resolution in the sub-

piconewton (pN) range. On the other hand, the maximal trapping force, which is determined by several factors such as the diameter and refractive index of the bead, the numerical aperture and geometry of the optical system, and the incident optical power, is typically smaller than 200 pN.

Applications of optical tweezers

Optical tweezers instruments exploit the optical force of light to trap small particles. Though the existence of optical force, or radiation pressure, has been theoretically demonstrated by Maxwell in 1873, its experimental demonstration had to wait until the turn of the century. The reason for this lapse is that radiation pressure is very feeble. Milliwatts of power impinging on an object result in piconewtons of force. In 1960s, the advent of lasers began to offer researchers the possibility to study radiation pressure through the use of intense, high collimated sources of light.

In 1970, A. Ashkin demonstrated that tiny particles such as small dielectric spheres could be trapped and manipulated by employing two counter-propagating laser beams and predicted the optical manipulation of atoms and molecules. An alternative optical trapping scheme, reported in 1986 (Ashkin *et al.*, 1986) simply consisted of bringing a beam of laser light to a diffraction-limited focus using a microscope objective. In the right conditions, the intensity gradient of light near the focal region can achieve stable three dimension trapping of dielectric object. The term *optical tweezers* was coined to describe this single-beam scheme. In 1987 Ashkin and collaborators showed that optical tweezers could manipulate living specimens such as bacteria, viruses (Ashkin & Dziedzic, 1987) and cells (Ashkin *et al.*, 1987; Ashkin & Dziedzic, 1989) and that through the proper choice of wavelength, optical damage to biological samples could be minimize, opening the doors to the possibility to apply optical tweezers to a wide range of biological systems.

Since its implementation, the optical tweezers have been utilized to study the kinetic and mechanical properties of single molecules. Generally, in these experiments a micro-sized bead, used as a handle attached to the molecular system under investigation, is manipulated with optical tweezers. The biophysical properties and dynamic structures of the double stranded DNA have been investigated attaching two microbeads to either ends of a ds-DNA molecule, one

was held by suction on the tip of a micropipette and the other manipulated with optical tweezers. Using this configuration, Smith *et al.* (1996) have shown that ds-DNA of λ phage undergoes a highly cooperative structural transition, overstretching transition, at a force of ~65 pN. Recently, the DNA overstretching transition has been reinvestigated with a dual laser optical tweezers provided with a fast force clamp system (Bianco *et al.*, 2011) which opened the possibility to directly determine the kinetics of overstretching transition.

Optical tweezers have been extensively employed to study the mechanics of motor proteins. The movement generated by conventional kinesin has been studied by trapping and tracking a kinesin-coated silica bead with optical tweezers (Svoboda *et al.*, 1993). These experiments showed that the processive motor kinesin moves along microtubules with steps of 8 nm. With a similar approach and finely controlling the load applied to the molecule, the force-velocity relation of kinesin has been described (Svoboda & Block, 1994). In these experiments kinesin velocity (stepping frequency) decreases linearly with increasing force and stops at a load of ~6 pN (stall force).

Muscle myosin II is not a processive motor and spends a large fraction of the ATPase cycle time detached from actin, thus the method of single molecule measurement must be adapted to prevent the motor from flying away under the effect of thermal agitation when it is detached. The most used experimental configuration to study the mechanics of myosin II with optical tweezers is the three bead assay, TBA (Fig. 1.11). In this approach, an actin filament is suspended between two beads trapped in two distinct optical traps and brought into contact with a single myosin molecule adsorbed on the surface of a third bead (Fig. 1.11A). In this way brief actomyosin interactions are detected by the reduction of the noise of the bead position due to the increased stiffness of the system (Fig. 1.11B). Using this configuration the step movement and the force produced by single myosin molecules (Finer *et al.*, 1994) and S1 fragments (Molloy *et al.*, 1995) have been measured. The values measured were 11 nm movement and 4 pN force for the myosin and 4 nm movement and 4 pN force for S1. Another important mechanical parameter that can be measured with TBA is the stiffness of the myosin molecule. Once the compliance of actin-bead links is taken into account the values for stiffness of rabbit HMM (Veigel *et al.*, 1998) and pure fast and slow

isoforms of rat myosin (Capitanio *et al.*, 2006) were 0.7 pN·s^{-1}, 0.9-1.4 pN·s^{-1} and 0.35-0.4 pN·s^{-1} respectively.

During its transient interaction with an actin filament, myosin generates a unitary filament displacement or working stroke (*d*). *d* for both non muscle myosin I (Veigel *et al.*, 1999) and smooth muscle myosin (Veigel *et al.*, 2003) has been found to be composed of two steps. The first 6 nm step, occurring immediately after the myosin binding to actin, was attributed to the conformational change coupled with the Pi release. The second step, smaller in amplitude, was attributed to a conformational change in the myosin head promoted by ADP release (Veigel *et al.*, 1999; Veigel *et al.*, 2003). Recently, using a system with higher time resolution and low ATP concentration (< 50 μM), it has been shown that also muscle myosin II performs the working stroke through two steps (Capitanio *et al.*, 2006). However. the high speed of the muscle myosin working stroke, the short lifetime of its interaction with actin and the large series compliance intrinsic to the TBA, makes muscle myosin kinetics difficult to be measured in single molecule experiments. In this respect, a step forward has been done maintaining the actin filament pre-loaded (Capitanio *et al.*, 2012) with the TBA configuration under force clamp control, so that upon binding, the myosin immediately experiences the load on the actin filament. In this way the temporal resolution of the system has been greatly improved and interactions as brief as 100 μs can be detected. However, also with this version of TBA, due to interaction speed of myosin II, the size and rate of the working stroke can be measured only at [ATP] of 50 μM at maximum,

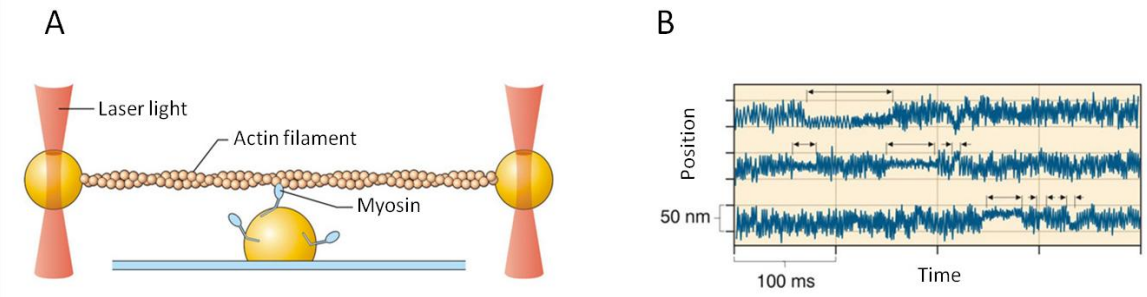

Fig. 1.11. The three bead assay. **A.** Schematic representation of the experimental set up. Each end of a biotinylated actin filament is attached to a streptavidin coated bead. The beads are held by two different optical tweezers and the actin filament is brought into contact with a third bead coated with myosin molecules. The myosin concentration on the bead is low enough to guarantee the interaction of a single myosin molecule with the actin filament. **B.** Typical experimental traces of bead position obtained projecting the image of the beads onto a charge-coupled device camera. The myosin bonds to actin are detected by the reduction of Brownian motion. The difference between the mean positions of the bound state and unbound state measures the myosin working stroke size.

much lower than the physiological value, preventing the possibility for the method to resolve the mechano-kinetics of the motor under physiological conditions.

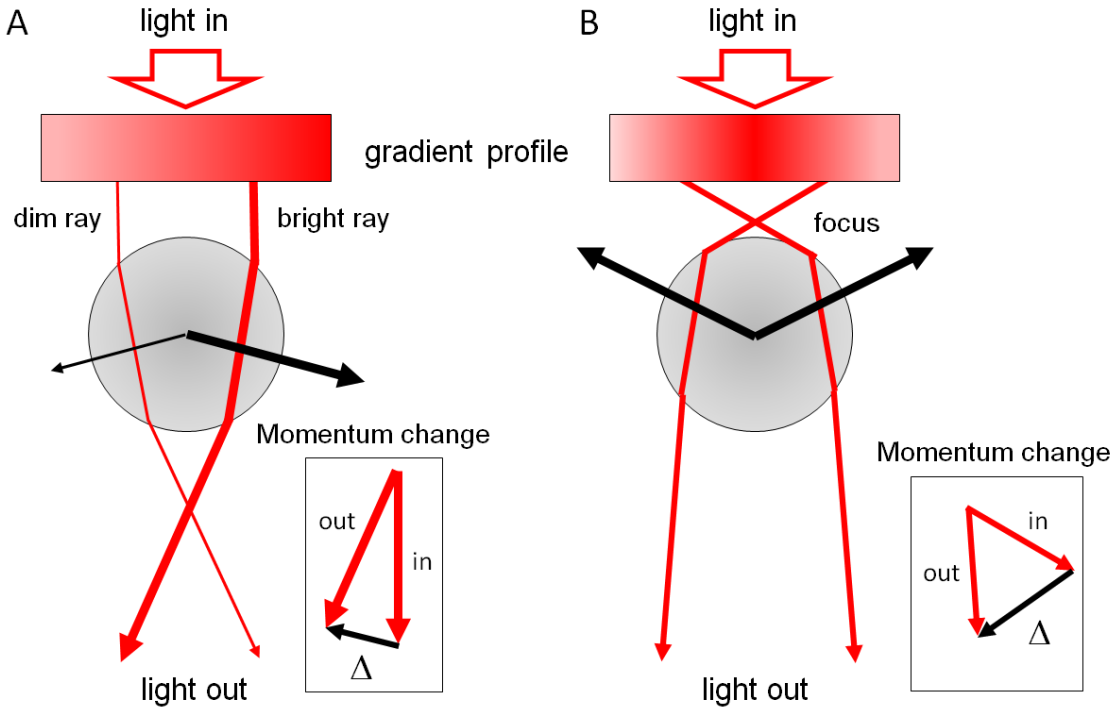

Fig. 1.12. Geometric optics of gradient force and single beam optical tweezers in the Mie regime. **A.** Ray-optic picture of the gradient force. A parallel beam of light (white arrow) with a gradient intensity (shaded region, the darker color indicates higher light intensity) impinges the surface of a sphere with a higher refractive index than the surrounding medium. The relative thickness of the two representative rays (red arrows) symbolizes the difference in the intensity. The rays are refracted, generating the reaction forces acting through the sphere's center (black arrows). The brighter ray produces a force larger than the dimmer ray. The sum of all rays in the beam generates a gradient force that pull the sphere toward the brighter region of the light. (*inset*) Vector diagram indicating the change of momentum for the higher intensity ray. The difference in momentum (black arrow) generates a force equal and opposite on the sphere. **B.** Single beam optical trap. The light (white arrow) is brought into a focus through a converging lens (e.g. a microscope objective) and its beam profile has an intensity gradient (shaded region). The two representative rays (red arrows) are bent by the interaction with the sphere. The resulting forces (black arrows) pull the sphere upwards, towards the focus. (*inset*) Vector diagram indicating the change of momentum for the left ray. The difference in momentum (black arrow) generates an equal and opposite force on the sphere.

Theory of trapping

Radiation pressure utilized in optical trapping originates from the momentum change of photons as the light is adsorbed, emitted, scattered, or reradiated by matter. Radiation pressure can manifest itself in several way. Perhaps the most common form is the *scattering force*, which is defined as the force due to light scattering that is proportional to the light intensity and acts in the direction of light propagation. This force may also be regarded as a consequence

of the momentum delivered by scattered photons. However, in optical tweezers the trapping is due to the *gradient force* which is instead proportional to the spatial gradient of light intensity and acts in the direction of the gradient.

The origin of gradient force can be explained using geometric optics when the dimension of the trapped particle, *d*, is greater than the wavelength of light, λ, a condition referred to as the Mie regime (Fig. 1.12). Instead, when $d<\lambda$, the Rayleigh regime, the gradient force can be viewed as arising from the polarization of the particle induced by the electric field component of the light. The polarized particle is then attracted towards the highest intensity region of the field. Below we will focus on the Mie regime since most of the biological application of optical tweezers fall in this regime.

When a beam of light impinges the surface of a spherical particle with a refraction index higher than the surrounding medium, the rays of light are refracted so that their direction of propagation changes according to Snell's law. Since the rays of light carry a momentum, a change in their direction produces a change in their momentum. By conservation of momentum law, the rate of change of momentum in deflected rays conveys equal and opposite rate of change in the momentum to the spherical particle. The rate of change of momentum produces a force according to Newton's second law.

When a dielectric sphere is placed in a light gradient, the change in the momentum of all rays refracted at its surface generates an asymmetric force, tending to push the sphere towards the brighter region of light (Fig. 1.12A). When a beam of light is brought into a focus with a convergent lens as a microscope objective, its profile has an intensity gradient. In this case a dielectric sphere placed in the focused beam experiences a net force pointing towards the focus of the light (Fig. 1.12B). Thus in the absence of other forces, the sphere is stably trapped in the focal point of the light. Unfortunately, also the scattering force, due to the reflection of the light at its surface, acts on the sphere. This force tends to push the sphere out of the trap. To overcome this loss mechanism, the optical trap must be designed to have high trapping force. From what mentioned above it is clear that the rays of light coming from the edge of the microscope objective contribute the most to the trapping force. In practice this means that a microscope with a high numerical aperture must be used to generate the greatest trapping

force. For the same principle, overfilling the back aperture of the objective with the laser beam leads to a higher trapping force (Ashkin, 1992).

The principles mentioned above form the basis of the most commonly used single beam optical tweezers (Ashkin *et al.*, 1986). However, an alternative optical tweezers approach that can overcome the loss due to the presence of scattering force uses a dual-beam design (Ashkin, 1970) (Fig. 1.13). In this configuration, two microscope objectives face each other and focus two separate laser beams to the same spot (Dual-laser optical tweezers, DLOT). Since the scattering force due to reflection is approximately the same for each laser, these forces cancel out each other and the axial trap stability is greatly enhanced. Dual-laser optical tweezers are therefore able to generate higher trapping forces for a given laser power and can be constructed with lower NA microscope objectives. The disadvantage of such an instrument lies mainly in its complexity. While single-beam optical tweezers can be constructed using a single laser and a commercial microscope, a dual-beam instrument is typically custom-built from optomechanical components. Importantly, the two laser beams must be aligned to within less than a bead diameter and the resulting measurements must be corrected for errors due to the drift in the relative beam alignment. Because of these alignment issues, single-beam instruments are preferable for trapping beads of diameters less than one μm.

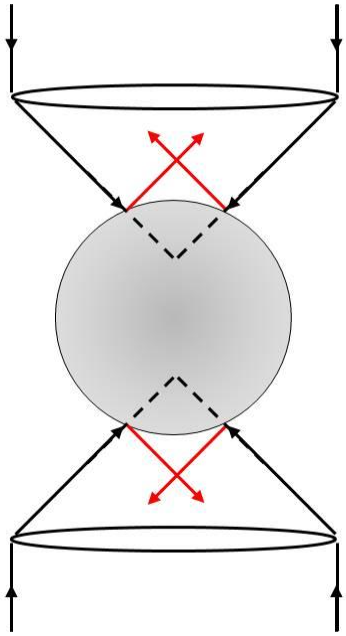

Fig. 1.13. Schematic representation of the scattering forces in the DLOT. The two pair of representative light rays (black arrows) are reflected (at the surface of the sphere (red arrows). On each side of the trap the scattering forces generated by the reflection are equal in amplitude and opposite in direction. Then the net scattering force acting on the bead is zero.

Measurement of force

Optical tweezers can be used to directly measure forces on trapped objects. If a refractive particle is held at some position away from the focus of the laser

beams, it experiences an attractive force towards the focus because of the action of gradient force described in the previous section. Thus, the potential well defined by the optical trap can be thought of as a spatially-defined virtual spring with a stiffness (spring constant) of k and the force acting on the trapped particle is proportional to the distance between the centre of the particle and the focus of the laser, Δx. In other words optical tweezers force, F_T, can be described by the equation:

$$F_T = -k \cdot \Delta x \qquad (1)$$

Thus, if the trap stiffness is known, measuring particle position allows the determination of the force acting on the bead. Modern image analysis techniques are able to measure the position of a micron-sized-bead with an accuracy of ~10 nm. Considering a value of ~0.1 pN·nm^{-1} for stiffness of common optical tweezers, ~ 1 pN force resolution may be reached. Hence the force resolution is increased by decreasing the trap stiffness. Other more sophisticated position sensing methods have been employed to increase the force resolution. In 1990, Denk & Webb used the optical interference pattern between beams displaced by small distance to determine the change in position of a bead in an optical trap. Bead position may also be measured with high precision by using quadrant photodetectors (Finer *et al.*, 1994) or projecting the position – in the condenser back focal plane – of the trapping laser, after it has left the optical trap, onto a position-sensing photodiode (Ghislain *et al.*, 1994). These approaches yield sub-piconewton force resolution.

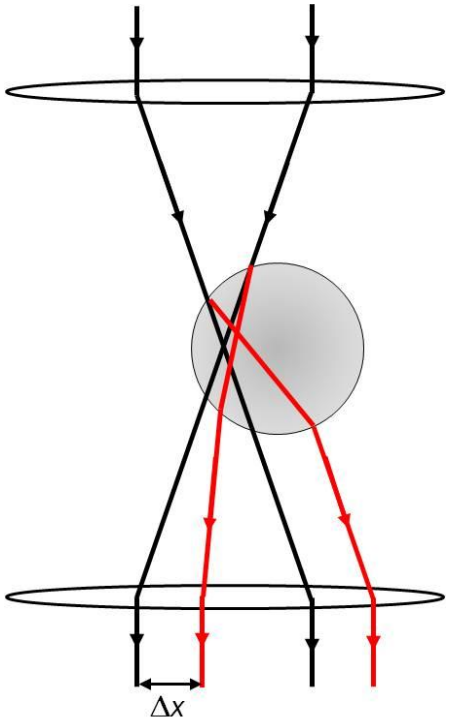

Fig. 1.14. Measurement of force on a trapped particle. In the dual-laser optical tweezers the back apertures of the objectives is underfilled. In this way, the trapping lasers can be used to measure the force on the trapped particle. The axial displacements of the laser beams (Δx) measure the change in light momentum and then the force on the particle.

In dual-laser optical tweezers, the trapping laser itself can be used to measure the force acting on a trapped particle. As shown in Fig. 1.14 laser light entering and exiting a refractive particle has its momentum changed by the presence of the particle. This momentum change, and thus the force acting on the particle, is equivalent to the change in the direction of propagation of the light, which can be directly measured by imaging the beam position using a position sensitive photodiode detector (Smith *et al.*, 2003). This method requires that all the photons entering the trap must be collected after they have left the trap. As a consequence the objective lens back aperture needs to be underfilled by the laser beam, decreasing the trapping force. However, a dual-laser optical tweezers instrument can sacrifice some trapping force considering the advantages of this approach for force measurement. Indeed, using this method the force calibration is independent of particle's size, shape or refractive index, its distance beyond the coverslip, the viscosity or refractive index of the buffer and variations in laser power (Smith *et al.*, 2003). In this work a dual-laser optical tweezers instrument is used because the dynamic range of force of a single laser (1-20 pN with a 900 mW laser) would be not adequate for the MYOMAC. Instead, with the same power laser, the dynamic range of the dual laser would be 1-200 pN, adequate to measure the force of MYOMAC.

1.2.8.3 Solution studies: Transient kinetics of motor proteins

It is generally accepted that the sequence of events in the actin-myosin ATPase cycle is essentially the same for all muscle myosin. The different properties among myosin isoforms can therefore be attributed to modulation of the rate constants and equilibrium constants of individual molecular events. The kinetics and equilibrium properties of single events of the ATPase cycle can be investigated using transient kinetic methods in which the reactants are mixed by means of a fast-mixing apparatus, such as the stopped-flow spectrophotometer, and the reaction is followed monitoring the changes in optical properties of the solution. Transient kinetics techniques have been applied to a large number of members of myosin family (Coluccio & Geeves, 1999; Bloemink *et al.*, 2007; Iorga *et al.*, 2007; Adamek *et al.*, 2008; Taft *et al.*, 2008; Bloemink *et al.*, 2011). As regards skeletal muscle myosin, the method has been used to investigate the

kinetic mechanism that determines the difference in maximum shortening velocity of fibres containing different myosin isoforms.

It has been proposed (Siemankowski & White, 1984; Siemankowski *et al.*, 1985) that the maximum shortening velocity of a single muscle fibre could be limited by the lifetime of strongly attached cross-bridges, that is controlled by the rate of cross bridge detachment. If a muscle fibre shortens at the maximum velocity V_0 and the working stroke size is d, then the lifetime of strongly attached crossbridges, τ, cannot be greater than d/V_0, without producing a drag on moving filaments. Thus $1/\tau$ is the minimum value of the rate constant (k_{min}) controlling cross-bridge detachment. This relation can be expressed as:

$$k_{min} = \frac{V_0}{d} \qquad (2)$$

Using transient kinetic approach, Siemankowski *et al.* (1985) have estimated the rate of release of ADP (k_{-ADP}) from the actin-myosin complex for a series of myosin isoforms isolated from different muscle types. They found a good correlation between k_{-ADP} and the unloaded shortening velocity (V_0) of the fibres and suggested that k_{-ADP} could define k_{min} and limit cross-bridge detachment and velocity of shortening. This idea was confirmed subsequently (Weiss *et al.*, 2001) for a wider range of myosin isoforms. Recently, the problem has been reinvestigated using HMM fragments from different pure myosin isoforms (Nyitrai *et al.*, 2006). Using HMM it could possible to study the biochemical transient kinetics of different myosin isoforms at ionic strengths comparable to those used for shortening velocity measurements in skinned fibres, enabling a simpler comparison of the values. It was found that the relative contributions of k_{-ADP} and k_{+ATP} in defining the shortening velocity could be different for the slow and fast isoforms at different temperatures and demonstrated that the rate of ATP induced actin-myosin dissociation plays a significant role in defining V_0 of fast isoforms in contrast with the original hypothesis that ADP determines V_0.

Transient kinetics studies on S1 from frog skeletal muscle (Ferenczi *et al.*, 1978a; Ferenczi *et al.*, 1978b) did not produce definitive results because of both the great lability of the frog proteins in those studies and the limited time resolution of the method. In this thesis, the kinetics of frog S1 has been reinvestigated under controlled temperature conditions using a high temporal resolution stopped-flow apparatus.

Chapter 2 – MATERIALS & METHODS

2.1 Preparation of proteins

2.1.1 Preparation of HMM and myosin S1 from frog skeletal muscle

Frogs (*Rana esculenta*) were kept in a humid environment at 4-6 °C for no longer than 2 months. The animals were sacrificed by decapitation followed by destruction of the spinal cord in agreement with the official regulation of the European Union (Directive 86/609/EEC) and with Schedule 1 of the UK Animals (Scientific Procedures) Act 1986. Muscle from thigh and legs were used because they contain mainly fast twitch fibres that are the source of a well-established set of mechanical and energetic data from frog skeletal muscle. A single frog provides about 3-4 g of muscle tissue from hind limb musculature. Myosin II was prepared following the protocols recently developed in the Laboratory of Physiology of Biology Department, University of Florence (Elangovan *et al.*, 2012).

S1 and HMM fragments were prepared by chymotryptic digestion of myosin II as follows. The purified myosin was precipitated adding 10 volumes of BED

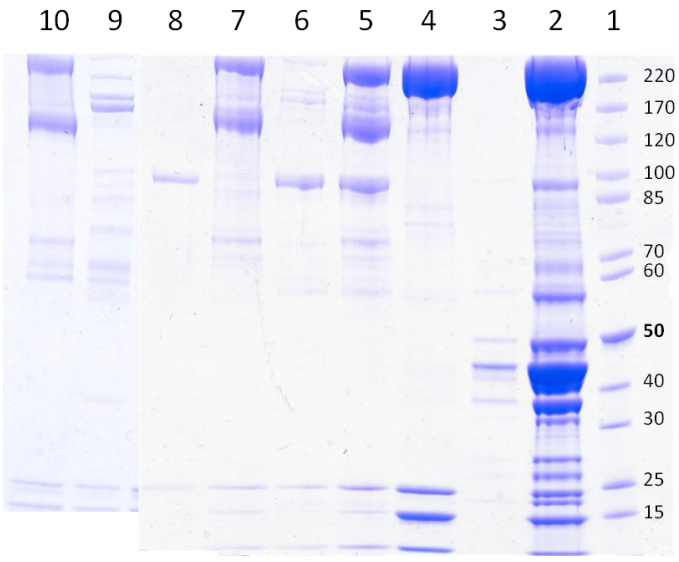

Fig. 2.1. SDS-PAGE gel showing the complete purification process of the myosin fragments, S1 and HMM, from frog skeletal muscle. Wells 2,3 and 4 refer to steps of the myosin purification and are common for both HMM and S1 purification processes.
1. Protein marker;
2. Proteins extracted from frog muscle;
3. Discarded supernatant of the myosin prep;
4. Purified myosin;
5. S1 prep: chymotriptic digestion;
6. S1 prep: Purified S1 fragment;
7. S1 prep: Undigested myosin and tails;
8. Rabbit S1 fragment;
9. HMM prep: Purified HMM;
10 HMM prep: Undigested myosin and tails

buffer ($NaHCO_3$ 0.1 mM pH 7.0, EGTA 0.1 mM and DTT 1 mM). After 10 minutes the solution was centrifuged at 10000 rpm for 30 minutes at 4 °C (centrifuge Allegra 25R Beckam coulter). The supernatant was discarded and the pellet (containing myosin) was dissolved with the digestion solution. For HMM purification the solution contained: KCl 750 mM, KPi 10 mM pH 6.5, $MgCl_2$ 2.5 mM, DTT 2 mM and EDTA-free antiprotease cocktail from Roche. For S1 purification the solution contained: KCl 750 mM, KPi 10 mM pH 6.5, EDTA 1 mM, DTT 2 mM and EDTA-free antiprotease cocktail from Roche. The digestion was performed on ice with constant gently stirring, adding to the solution α-chymotrypsin (Sigma Aldrich) to a final concentration of 0.2 $mg \cdot ml^{-1}$. After 3 hours for HMM and 2 hours for S1, phenylmethylsulfonyl fluoride (PMSF) to a final concentration of 2 mM was added to the solution to quench the reaction and the mixture was incubated for further 30 minutes with constant stirring on ice. Undigested myosin and insoluble myosin fragments were precipitated by dialysing the digestion mixture overnight in cold room against the dialysis buffer (KCl 30 mM, MOPS 20 mM pH 7.0, $MgCl_2$ 5 mM, DTT 2 mM). The HMM or S1 fragments were separated from the precipitated material by centrifuge at 13000 rpm for 15 minutes at 4 °C in a bench centrifuge. The pellet was discarded and the supernatant, containing the HMM or S1 was kept. The absorbance at 280 nm (A_{280}) was measured using a spectrophotometer and the protein concentration was calculated from the following equation:

$$C(\mathrm{mg \cdot ml^{-1}}) = \frac{A_{280}}{\varepsilon_{280} \cdot l} \cdot dilution \qquad (3)$$

where C is the protein concentration, ε_{280} is the protein molar absorptivity at 280 nm wavelength (HMM $\varepsilon_{280} = 0.65$ $\mathrm{ml \cdot mg^{-1} \cdot cm^{-1}}$) and l is the path length in cm.

The degree of purification of the fragment was checked by SDS polyacrylamide gel electrophoresis (Fig. 2.1).

2.1.2 Preparation of actin

G-actin was prepared from rabbit leg muscles using the procedure of Pardee and Spudich (1982). G-actin, frozen with liquid N_2, was stored at -80 °C and used for up to one year. G-actin was polymerised into F-actin by adding HEPES 20 mM, KCl 10 mM, $MgCl_2$ 2 mM, ATP 100 μM, β-mercaptoethanol 0.01%. F-actin was fluorescently labelled according to the method of Kron *et al*,

(1991) by incubating it overnight at 4 °C with excess of phalloidin-tetramethyl rhodamine isothiocianate (TRITC) (5:1 TRICT: actin molar ratio). Labeled F-actin was stored at 4 °C in aliquots covered with aluminium foils to avoid exposition to light and used for up one week. For the stopped flow experiments, the actin was selectively labelled with pyrene at cysteine 374 (pyr·actin) as described by Criddle *et al.* (1985) (the average labelling content was ~90%).

2.2 Transient kinetics experiments

2.2.1 Stopped-flow spectrophotometer

Biochemical kinetics of the myosin fragments were defined using the Stopped-Flow Spectrophotometer apparatus developed in Mike Geeves laboratory (University of Kent, Canterbury, Millar & Geeves, 1983). The typical Stopped-Flow Spectrophotometer (Figs 2.2 and 2.3) consists of two air-driven drive syringes (containing the reactants), mixing and observation chambers, a stop-syringe and a data recording and evaluation system.

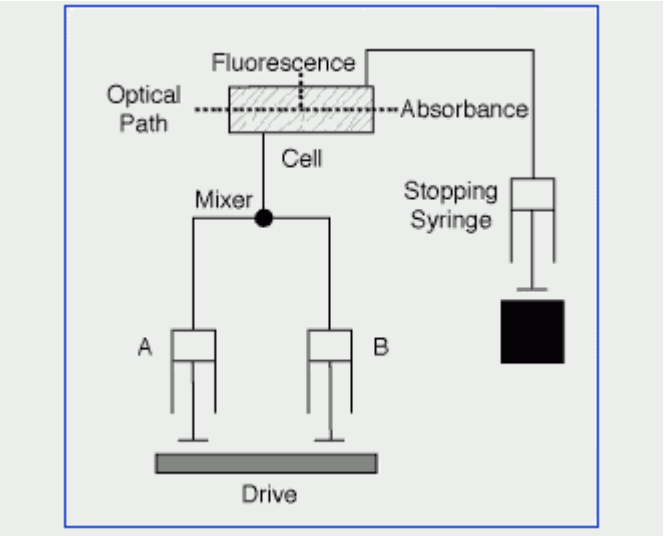

Fig. 2.2. Schematic set up of the stopped-flow apparatus. The two air-driven drive syringes force the reactants to enter into the mixing chamber and then the observation chamber. The reactions are followed monitoring the fluorescence or absorbance in the observation chamber. The mixed volume is defined by the stopping syringe.

The reaction was initiated by simultaneously triggering the drive syringes, forcing the reactants through the mixing device into the observation chamber. The reactants were mixed in ratio of 1:1. The volume mixed was determined by the set volume of the stop-syringe, which triggered the data recording by activating a micro switch. The observation chamber was equipped to measure either absorbance (and light scattering), or fluorescence changes in the reaction mix. By

manipulating the monochromator, photomultiplier and filters, the desired excitation and emission wavelengths were selected, while the data recording and evaluation system were adjusted for the optimal time scale of acquired data. Since the samples were mixed in a 1:1 ratio the actual enzyme/substrate concentration in the observation cell was halved.

Rapid kinetic stopped flow experiments were carried out on a stopped-flow system (model SF-61 DX2, Hi-tech Ltd., Salisbury, UK) fitted with a 75 watt Xe/Hg lamp and monochromator. This apparatus allowed controlling the temperature in both the mixing and observation chambers. Pyrene was excited at 365 nm, and emission was monitored at 389 nm (KV389 cut-off filter). All the transients shown are the average of 3-10 shots of the stopped-flow apparatus. Data were stored and analyzed using KinetAsyst software provided by Hi-Tech Scientific. The concentrations used to describe the experimental conditions in this thesis refer to the final concentrations in the stopped-flow reaction mixture. The standard error of the exponential fits is typically less than 1% of the estimated parameter.

Fig. 2.3. Image of the stopped-flow apparatus (left) fitted with the Xe/Hg lamp and monochromator (right).

2.2.2 Kinetic data analysis

The stopped flow was used to investigate the ATP induced dissociation of the actin – myosin S1 complex and the ADP affinity of myosin S1. The data

obtained were interpreted in terms of the model described in scheme 1. In this scheme the equilibrium constants of single reaction are indicated with capital letters while the rate constants are indicated with lowercase letters. In the proposed model, a very rapid equilibrium is reached between A·M and ATP after mixing actin-S1 with ATP, defined by the association constant K_1 and followed by isomerisation of the ternary complex (A·M·T), which limits the maximum rate of actin dissociation from the complex (k_{+2}) (Geeves *et al.*, 1986). Therefore, in the pseudo first order conditions, the observed rate constant for ATP induced actin-frogS1 dissociation (k_{obs}) is defined by the following equation:

$$k_{obs} = k_{+2} \frac{[ATP]}{\frac{1}{K_1} + [ATP]} \qquad (4)$$

For the fast isoform of skeletal muscle myosin, ADP is in rapid equilibrium with actin-S1 complex compared with the rate of ATP induced actin-S1 dissociation. In scheme 1 the ADP equilibration is controlled by K_{ADP}. Under these conditions, ADP and ATP compete effectively for A·M binding site and k_{obs}, for a fixed ATP concentration, is given by the following equation:

$$k_{obs} = \frac{k_0}{1 + \frac{[ADP]}{K_{AD}}} \qquad (5)$$

Where k_0 is the observed rate constant of ATP induced actin-S1 dissociation in the absence of ADP and defined by equation (4). K_{ADP} represents the affinity of actin-S1 complex for ADP, and is expressed as dissociation constant: $K_{ADP} = k_{+ADP}/k_{-ADP}$

.

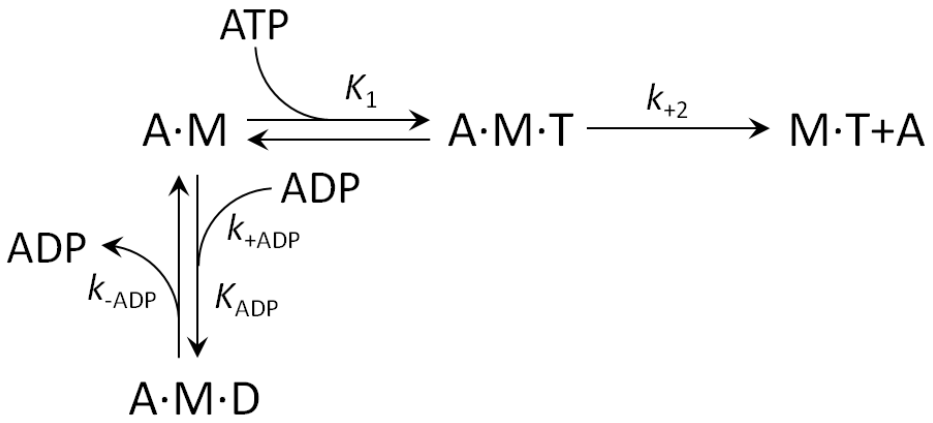

Scheme 1. Proposed model for ATP induced dissociation of actin·frogS1 complex in the absence and presence of ADP. ATP is in rapid equilibrium with A·M and the rate of dissociation reaction (k_{+2}) is limited by the irreversible isomerisation step. ADP competes with ATP for the A·M binding site. M=S1; A=actin;T=ATP; D=ADP.

2.2.3 Thermodynamic data analysis

The ATP-induced actin-S1 dissociation experiments were carried out at different temperatures to have the constrains to define the thermodynamic parameters (enthalpy and entropy) of the reaction. The effect of temperature on the equilibrium constant K_1 was displayed in the Van't Hoff plot ($\ln K_1$ versus 1/absolute temperature) and fitted with the Van't Hoff equation to estimate the enthalpy ΔH^o and the entropy ΔS^o of the reaction:

$$\ln K_1 = -\frac{\Delta G^\circ}{R \cdot \mathrm{T}} = -\frac{\Delta H^\circ}{R} \cdot \frac{1}{\mathrm{T}} + \frac{\Delta S^\circ}{R} \qquad (6)$$

where $\Delta G^\circ = \Delta H^\circ - T \cdot \Delta S^\circ$, R is the molar gas constant, T is the temperature in Kelvin, ΔH^o is the reaction enthalpy (standard state) and ΔS^o is the reaction entropy (standard state).

The activation energy of the dissociation reaction was defined by investigating the effect of temperature on the rate of the reaction k_{+2} and plotting $\ln k_{+2}$ as a function of 1/absolute temperature. The plot was analyzed using the Arrhenius equation:

$$\ln k_{+2} = -\frac{\Delta G^\ddagger}{R \cdot \mathrm{T}} + \ln\left(\frac{k_B \cdot \mathrm{T}}{h}\right) = -\frac{\Delta H^\ddagger}{R} \cdot \frac{1}{\mathrm{T}} + \frac{\Delta S^\ddagger}{R} + \ln\left(\frac{k_B \cdot \mathrm{T}}{h}\right) \qquad (7)$$

where $\Delta G^\ddagger = \Delta H^\ddagger - \mathrm{T} \cdot \Delta S^\ddagger$, R is the molar gas constant, T is the temperature in Kelvin, k_B is the Boltzmann constant, h is the Planck constant, $\Delta H^\ddagger$ is the activation enthalpy and $\Delta S^\ddagger$ is the activation entropy.

2.3 IVMA experiments

2.3.1 Preparation of the flow cell for IVMA

The flow cell was prepared based on Spudich and collaborators method (Kron & Spudich, 1986), Nitrocellulose 0.1% dissolved in pentyl acetate was smeared on the coverslide and allowed to dry. The treated coverslide was mounted over the microscope slide with double sticky tapes as spacers, to delimitate a flow cell. The flow cell was kept on ice. The solution in the flow cell was changed by adding from one side with a pipette while sucking by capillary action from the other side with filter paper.

For the IVMA tests with different substrates the HMM adsorbing surfaces were prepared as follows. The TMCS derivatized coverslips were obtained by exposing the coverslip to vaporized TMCS (Sigma Aldrich) for about 10 minutes. The PMMA surfaces were prepared by cutting directly a piece of PMMA with the same dimension (24 x 60 mm) as a glass coverslip.

In the experiments with a saturating density of HMM on the surface, HMM 0.5 $mg \cdot ml^{-1}$ solution was incubated into the flow cell for 5 minutes. For experiments with varying HMM surface density, HMM concentration of the incubation solution was varied. After HMM incubation, the unbound HMM was washed away with a solution containing BSA 1 $mg \cdot ml^{-1}$. Then the flow cell was perfused with TRICT labelled F-actin (diluted in AB-buffer, 1:1000) and incubated for 2 minutes. The reaction mix with final desired pH, ionic strength, temperature, MgATP along with methylcellulose 0.5%, anti-photobleaching agents Catalase (20 $\mu g \cdot ml^{-1}$) and Glucose oxidase (100 $\mu g \cdot ml^{-1}$), Glucose (5 $mg \cdot ml^{-1}$) and DTT (10 mM), was added and the flow cell was sealed with silicon grease. After adding the reaction mix with MgATP the flow cell was mounted in the apparatus for data acquisition. In the case of low ATP concentration (<100 µM), the ATP regeneration system was also added (creatine phosphate 0.1 mM, creatine phosphokinase 10 $\mu g \cdot ml^{-1}$).

2.3.2 Composition of the solutions

The composition of the experimental base buffer in control conditions was: Imidazole, 25 mM (pH 7.5 at 25 °C), KCl 33.5 mM, $MgCl_2$ 4 mM, EGTA 1 mM, saturating free MgATP (2 mM), ionic strength 60 mM, pH 7.5 at room temperature (~ 25 °C). The ionic strength value of 60 mM was chosen from the data in literature

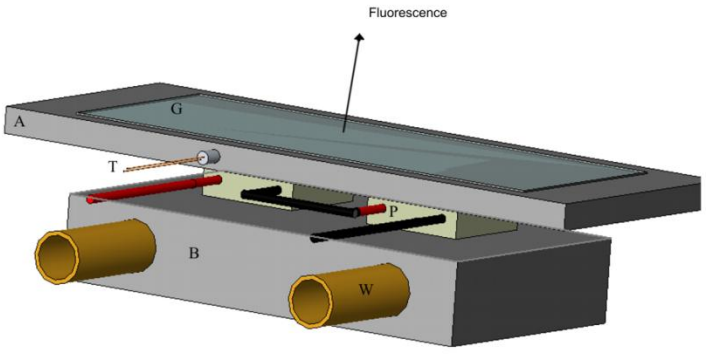

Fig. 2.4. Schematic representation of the temperature controller. G: Glass slide, A: aluminium plate, P: thermoelectric modules, T: thermistor, B: heat sink for the hot surface of the modules, W: pipes for the circulating water. The arrow indicates the direction of the fluorescence signal.

(Homsher *et al.*, 1992; Elangovan *et al.*, 2012). The value is smaller than the physiological value because at ionic strength above 60 mM the motility quality decreases due to the diffusion of actin filaments away from the surface. Base solutions were made 2x concentrated and diluted to reach 1x concentration in the assay. The pH of the solutions was adjusted at the final temperature. Methylcellulose 0.5% w/v was added to the flow cell solution, to increase solution viscosity and reduce actin diffusion, thus increasing the probability of interaction of actin filaments with myosin (Uyeda *et al.*, 1990). Methylcellulose was prepared in stock solution with concentration of 1.2% by dissolving it in water and dialysing overnight to ensure the complete solubility.

2.3.3 Temperature controller

The temperature of the IVMA flow cell was continuously monitored with a negative temperature coefficient (NTC) thermistor glued to the aluminium plate carrying the flow cell. The thermistor provided the feedback signal for a temperature control circuit, the output of which fed two thermoelectric modules (Melcor, CP 1.4-1.71-10L) stuck to the bottom of the aluminium plate carrying the flow cell (Fig. 2.4). The sink for the hot surface of the two thermoelectric modules was made of an aluminium chamber with cold water circulation. The temperature inside the flow cell, measured with an independent miniature thermocouple probe, differed from that of the aluminium plate by less than ± 0.5 °C in the whole range of temperature used.

2.3.4 Fluorescence imaging and data acquisition

The images of the fluorescent actin filaments have been recorded exploiting the fluorescence dedicated optical line of the dual laser optical tweezers (DLOT) (Bianco *et al.*, 2011) (Fig. 2.5). The optical line for the fluorophore excitation was composed by a laser Melles Griot MGL 532 (532 nm wave length, 100 mW power) and a band-pass filter (Semrock, FF01-542/20-25 CW 542 nm). The laser power at the sample level was a few milliwatts, to obtain an optimal compromise between high fluorescence signal and low photobleaching rate. The fluorescence signal collection was maximized by using an objective with high numerical aperture (NA) (Nikon PlanApo water immersion 1.2 NA), an high efficiency EEV CCD camera (Princepton Instrument Inc., Pentamax system), efficient filters and dichroic mirrors

with high quantum yield and transmission spectra optimized for TRITC. The sensitive surface of the EEV CCD camera was 7.7x7.7 mm (512x512 pixel CCD with single pixel dimension of 15x15 µm) with very high quantum efficiency and could attain high signal to noise ratio (S/N) even at fast acquisition rates (5 MHz). The magnification of the fluorescence image was ~300x, corresponding to 80 nm per pixel. Movies, made by sequences of images with 250 ms exposure time, were recorded and stored in the computer for further analysis.

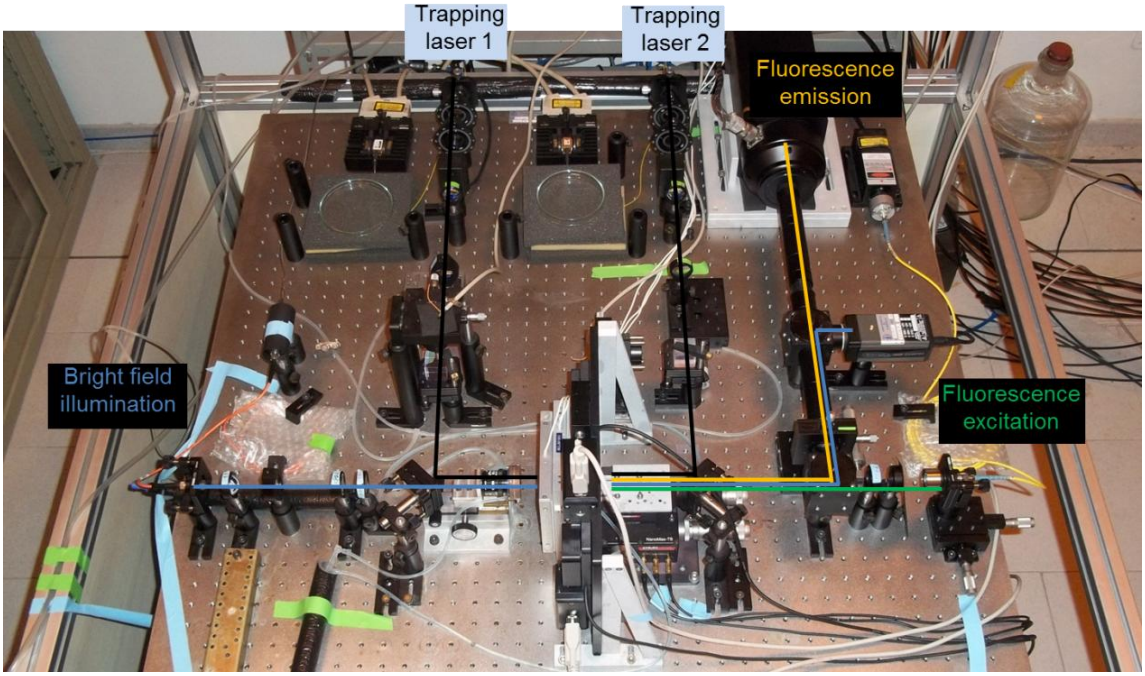

Fig. 2.5. Image of the DLOT. The continuous lines represent the optical paths of the DLOT. Black: optical line of the two infrared lasers that generate the optical tweezers (845 nm); Cyan: optical line of the bright field illumination (470 nm); Green: optical path of the green laser used for the fluorophore excitation (532 nm); Orange: optical path for the fluorophore emission (580 nm), with the fluorescence camera at the end of the path.

2.3.5 Data analysis

2.3.5.1 Tracking of filaments

Actin filament tracking was accomplished by analysing sequences of images with a custom built program developed with LabVIEW software (national Instrument). Background fluorescence was excluded by setting a threshold for the intensity in each pixel: the intensity was assumed to be zero in the pixels with intensity values below the threshold, whereas pixels with intensity values above threshold were unaltered. The threshold value was set so that the objects

remaining in view were only actin filaments. Filament velocity was calculated with the method of the centroid movement, determining the change in the position of the centre of mass of the actin filament under inspection in two successive images according to the equation:

$$C_x = \frac{\sum_{i=1}^{n}\sum_{j=1}^{m} x_i I_{ij}}{\sum_{i=1}^{n}\sum_{j=1}^{m} I_{ij}} \quad \text{and} \quad C_y = \frac{\sum_{i=1}^{n}\sum_{j=1}^{m} y_i I_{ij}}{\sum_{i=1}^{n}\sum_{j=1}^{m} I_{ij}} \qquad (8)$$

where C_x and C_y are the centroid coordinates, x_i and y_i are the coordinate of the i^{-th} pixel on the x axis and on the y axis and I_{ij} is the intensity corresponding to that pixel.

Playing the movie backward and forward, smoothly sliding filament were selected manually by eye and each selected filament was analysed individually. The filament was selected by choosing a rectangle around the actin filament. The position of the centroid of the filament in the first frame was calculated according to equation (8). The position of the centroid of the same filament in the next frame was found by enlarging the filament box from the previous position and using the equation again. This tracking process was continued for all frames selected. After determining the centroid position in successive frames, the frame-to-frame velocity of the actin movement was calculated as the distance moved between two consecutive frames multiplied by the frame frequency (Homsher *et al.*, 1992). The centroid position in each frame and length of the filament were stored for further analysis.

To be considered representative of the sliding velocity *in situ*, the filament movement had to match a quality level established according to the following two criteria (Homsher *et al.*, 1992): (*i*) a minimum distance of continuous movement (> 2 μm) and (*ii*) a minimum value (cut-off) of the ratio SD/mean, that is 0.3 depending on the framing rate, 5 Hz.

According to the criteria mentioned above only filaments showing smooth continuous movement were used for the analysis to estimate V_F because only in this case V_F could be comparable to the fibre unloaded shortening velocity (V_0).

2.3.5.3. Estimate of V_F

The mean sliding velocity and its standard deviation were obtained by fitting, with a Gaussian equation, the distribution of the values collected from the analysis of the frame-to-frame velocity in each filament:

$$n = Y_0 + Ae^{\frac{(V-V_{mean})^2}{2\sigma^2}} \qquad (9)$$

where n is the number of measurements, V is V_F determined frame to frame, V_{mean} is the mean of the distribution, σ is the standard deviation of the distribution, Y_0 and A are constants used for fitting.

2.4 Mechanical measurements on a limited ensemble of myosin motors

2.4.1 Preparation of the bead tailed actin

For the array of motors to exert force pulling the actin filament away from the trap, the filament must be attached to the bead with the (+) end (barbed end). The bead tailed actin (Fig. 2.6) was prepared on the basis of the protocol developed by Suzuki *et al* (1996). Bovine plasma gelsolin (Sigma Aldrich) was cross-linked to the carboxylated polystyrene bead (1-2 μm in diameter, Kisker Biotech GmbH & Co. KG) with 1-ethyl-3-(3-dimethylaminopropyl)-carbodiimide (EDC, Sigma Aldrich).The average number of actin filaments attached to the bead was controlled by crosslinking an appropriate amount of bovine serum albumin

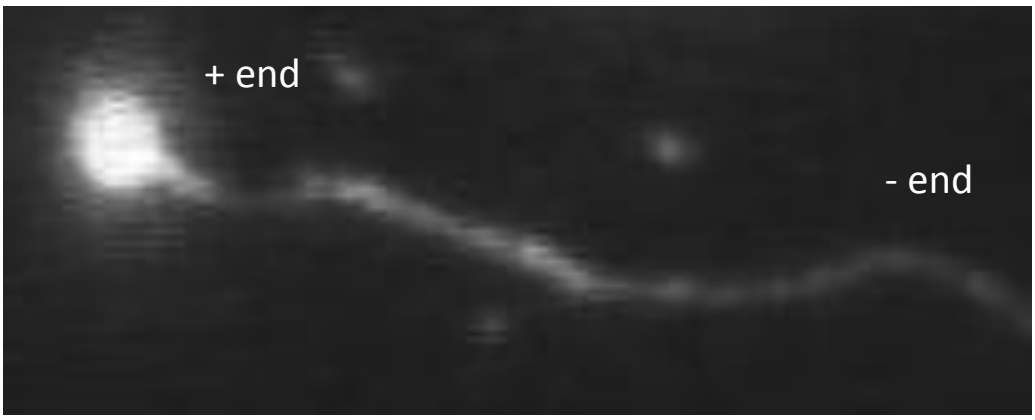

Fig. 2.6. Fluorescent image of a bead-tailed actin filament with the right polarity to be pulled by tl myosin array. Bead diameter 1 μm, actin filament length ~14 μm.

(BSA) to the bead. The bead was washed with a modified AB-buffer (Imidazole 25 mM pH 7.4; KCl 25 mM, $MgCl_2$ 4 mM, $CaCl_2$ 0.1 mM, ATP 0.1 mM, DTT 1 mM and NaN_3 3 mM) and mixed with 0.2 $mg \cdot ml^{-1}$ actin filaments labelled with rhodamine phalloidin (Sigma Aldrich). Before infusion into the flow cell, bead-tailed actin filaments were diluted in modified AB-buffer containing 1 $mg \cdot ml^{-1}$ BSA to avoid adsorption of the bead to the glass surface. Our measurements indicate that the strength of the bead-gelsolin-actin chain is > 100 pN and thus it is adequate for the force range generated by the motor ensemble.

2.4.2 Preparation of the support for the ensemble of HMM

In the final version of MYOMAC the support holding the motors will consist in a nanostructured surface obtained by grating the tip of an etched optical fibre by focused ion beam.

A simplified version of the MYOMAC for the preliminary measurements reported here provides that the number of HMM interacting with the actin filaments is limited by using as support the flat tip of the etched fibre (3-8 μm in diameter). The etched fibres were prepared in the laboratory of Dan Cojoc at IOM, CNR (Trieste) as follows. Single mode optical fibres for wavelengths from 450 to 1500 nm were etched in 40% hydrofluoric acid solution for 40 min to remove the cladding and shape the core of the fibres. Fibres for 800 nm have been found to be the best in order to obtain, by etching, a flat substrate with diameter of ~5 micrometers and a relatively large cone angle.

2.4.3 DLOT set up for mechanical measurements

The mechanical output of the MYOMAC is measured using a DLOT (Fig 2.5) (Smith *et al.*, 1996) that allows force measurements in the range of 0.5-200 pN and movement in the range of 1-70,000 nm. In the DLOT two counter propagating diode lasers (150 mW, 845 nm, THORLABS, Inc., Germany) are used to form a single optical trap in the experimental flow cell. The two laser beams have orthogonal polarizations, which allow their optical paths to be separated using polarizing beam splitters. The two laser beams are focused in the experimental flow cell through two water immersion objectives (Olympus, UPLSAPO 60XW, NA 1.20). The light exiting from each of the two objectives is projected on two position-sensitive detectors (PSD), which monitor the XY and Z

force components acting on the trapped bead. The force is measured using the conservation of photon momenta (Smith *et al.*, 2003).

For mechanical measurements on the myosin based machine, the actin filament was attached to the trapped bead acting as the force transducer and the optical fibre with the array of myosin motors was joint to the flow chamber the position of which is controlled by a 3-way piezoelectric nanopositioner acting as a motor length transducer. Bright-field microscopic images of the beads and fibre, illuminated with a blue LED (470 nm), were detected using a ¾ inches CCD camera (Bitron VIDEO). Two National Instruments boards were used for instrument control and data acquisition. A PCI 6030E board with 8 digital channels, an upper frequency limit of 100 kHz, was used for data generation and acquisition. Second, a PCI 6703 board was used to align the lasers and to modulate the pressure in the flow cell by controlling solenoid valves. Data acquisition was controlled by using custom-written LabView algorithms.

The system was implemented with (*i*) a temperature control of the flow cell and (*ii*) a rapid force clamp mode (Bianco *et al.*, 2011). The control can be switched from length-clamp mode to force-clamp mode by exchanging the feedback between the signal from the stage positioner controlled by the piezoelectric nanopositioner and the signal from the trapped bead. The frequency response of the system is limited by the rise time of the piezoelectric stage (t_r, measured from 10 to 90% of the step). t_r has been minimized to ~2 ms with a new stage (PDQ375, Mad City Lab, Madison WI, USA.) with dedicated electronics specifically devised in collaboration with the Mad City Lab technical staff.

2.4.4 Flow chamber for mechanical measurements

The experimental flow chamber was made by two coverglass slides separated by two layers of parafilm cut in order to obtain two streams of flow inside the chamber (Fig. 2.7). In this way it is possible to obtain two compartments, one used for mechanical measurements, where the etched optical fibre is mounted, and the other used to introduce the BTA. Separated compartments allow avoiding uncontrolled protein interactions. The chamber is sealed to withstand the fluid pressure by heating the two parafilm layers.

Since the distances between the compartments inside the flow cell are on the scale of the centimeters, the movements of the chamber-nanopositioner

system is brought to the adequate range by mounting the piezoeletric stage on an automated micropositioner that is able to generate 2-axes motion up to 25 mm (MicroStage series, Mad City Lab, Madison, WI) (Fig. 2.5).

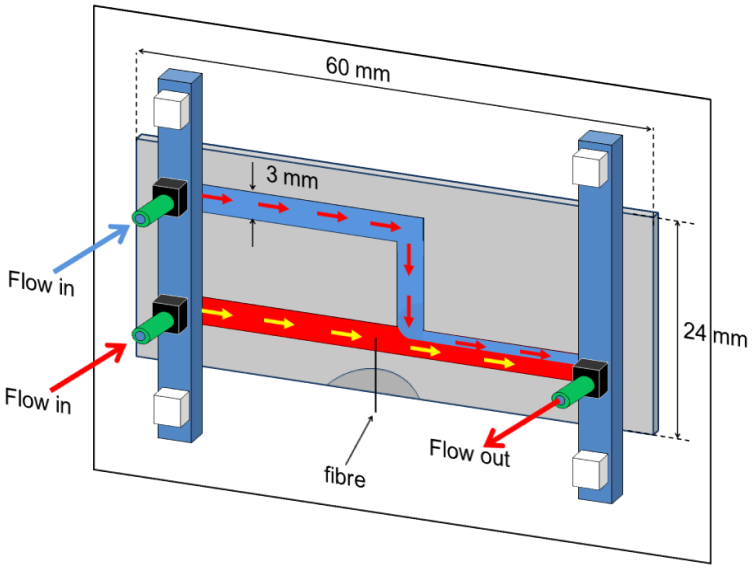

Fig. 2.7. Schematic representation of the experimental chamber. In the chamber, the flow that comes from the upper stream (blue and red arrows) and the one that comes from the lower stream (red and yellow arrows) remain separated, since they have the same pressure. This allows two distinct compartments to be generated. The etched optical fibre is mounted, in the lower compartment, upstream the intersection of the flows. The dimensions of the flow chambers are reported in the figure.

Chapter 3 – RESULTS

3.1 Transient kinetics studies on the fragments from frog myosin

3.1.1 ATP induced dissociation of actin-S1 complex

For transient kinetics studies, S1 is preferred to HMM because the total ATPase activity of myosin molecule resides in the S1 fragment, while it also has a higher solubility.

In the absence of ATP the S1 fragment forms a tight stable complex with actin. This complex can be rapidly dissociated adding ATP to the solution. Actin-S1 complex dissociation kinetics can be conveniently followed by monitoring the increase in fluorescence of pyrene-labeled actin (pyr·actin). Fig. 3.1A shows the fluorescence transient observed at 5°C when 1 μM actin-frogS1 is mixed with 20 μM ATP in the stopped flow spectrophotometer. The observed transient is well described by a single exponential equation with an observed rate constant (k_{obs}) of

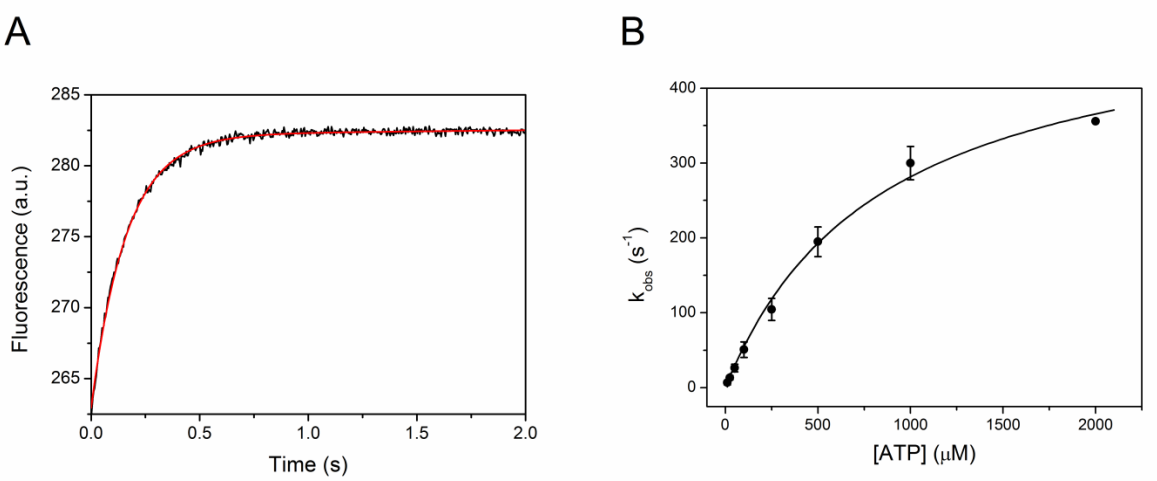

Fig. 3.1. ATP-induced dissociation of pyr·actin-frogS1 at 5°C. **A.** Fluorescence transient obtained mixing 1 μM pyr·actin-frogS1 with 20 μM Mg·ATP. The transient was fitted with a single exponential equation (continuous red line). **B.** Relation between k_{obs} and [ATP]. The data points were obtained from 3 different S1 preparation. Continuous line is the hyperbolic fit to the data with equation (4). The estimated parameters were: $1/K_1$ = 849 ± 111 mM, k_{+2} value of 527 ± 31 s^{-1}. Experimental conditions:5°C, 100 mM KCl, 20 mM cacodylate pH 7.0, 5 mM $MgCl_2$ and 1 mM NaN_3.

6.15 ± 0.04 s^{-1} and amplitude of ~7%. At 5°C k_{obs} shows a hyperbolic dependence on [Mg·ATP] according to equation (4) (Fig. 3.1B). The hyperbolic fit to the data gives an equilibrium constant $1/K_1$ of 849 ± 111 μM and a k_{+2} of 527 ± 31 s^{-1}.

The rate of ATP-induced dissociation was determined in the range of temperatures between 5 and 15°C. In Fig. 3.2A are shown the fluorescence transients obtained mixing 1 μM pyr·actin-frogS1 with 50 μM ATP at 5, 10 and 15°C. At all temperatures the transient is well described by a single exponential equation and k_{obs} is 10.70 ± 0.18 s^{-1}, 16.28 ± 0.14 s^{-1} and 32.09 ± 0.34 s^{-1} for 5, 10 and 15°C respectively. k_{obs} values are plotted as a function of [Mg·ATP] at each temperature in Fig. 3.2B.

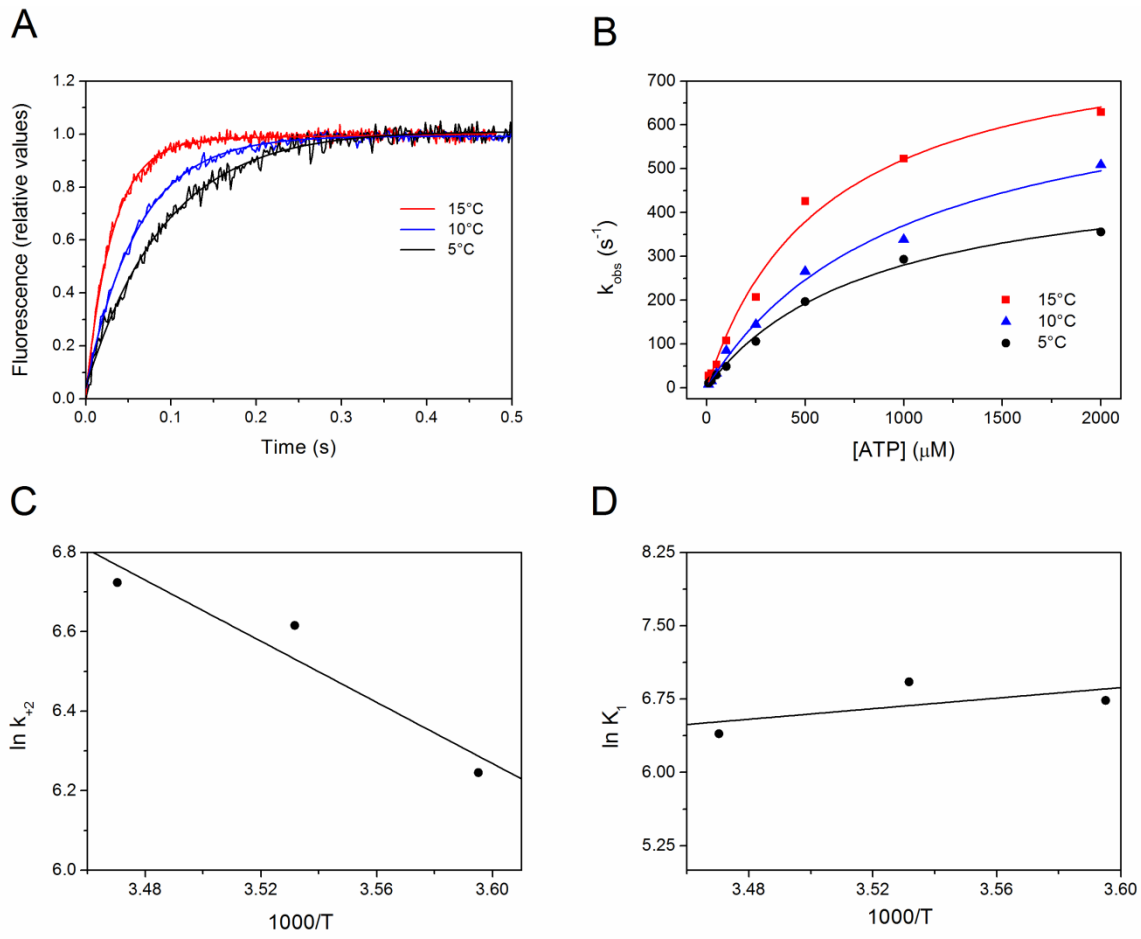

Fig. 3.2. ATP-induced dissociation of pyr·actin-frogS1 and its temperature dependence. **A.** Pyrene fluorescence transient of 1 μM pyr·actin-frogS1 mixed with 50 μM ATP at 5, 10 and 15°C. Continuous lines are the fit of the traces with a single exponential equation. **B.** k_{obs} dependence on ATP concentration at 5, 10 and 15°C. The data were obtained from the same S1 preparation. k_{+2} and $1/K_1$ at each temperature were estimated from hyperbolic fits with equation (4) (continuous lines); **C.** Arrhenius plot of k_{+2}. $\Delta H^{\ddagger}$ and $\Delta S^{\ddagger}$ were derived from the slope and the intercept of the linear fit, respectively. **D.** Van't Hoff plot of $1/K_1$. ΔH°, ΔS° were derived from the slope and the intercept of the linear fit, respectively. Experimental conditions: 100 mM KCl, 20 mM cacodylate pH 7.0, 5 mM MgCl2 and 1 mM NaN3.

	5°C	10°C	15°C
k_{+2} (s^{-1})	515 ± 25	746 ± 63	832 ± 57
$1/K_1$ (μM)	841 ± 91	1071 ± 177	598 ± 101

Table 1. Kinetics parameters (mean ± SE) of the ATP induced dissociation of pyr·actin-frogS1 at different temperatures.

In the range of temperatures used, k_{obs} shows a hyperbolic dependence on ATP concentration according to equation (4) and the hyperbolic fit to data gives the estimates of k_{+2} and $1/K_1$ (Table 1). At temperatures above 15°C, the relation could not be reliably determined because k_{obs} values at high [Mg·ATP] were too fast to be measured with the required precision.

The maximum dissociation rate constant k_{+2} increases from ~500 s^{-1} at 5°C to ~850 s^{-1} at 15°C. An Arrhenius plot of the data (ln k_{+2}:1/T, where T is the absolute temperature) is shown in Fig. 3.2C. The parameters $\Delta H^{\ddagger}$ and $\Delta S^{\ddagger}$ obtained by fitting Arrhenius equation (equation (7)) to data are listed in Table 2. The activation enthalpy ($\Delta H^{\ddagger}$ ~32 kJ·mol^{-1}) and activation entropy ($\Delta S^{\ddagger}$ ~170 J·K^{-1}·mol^{-1}) are positive and in agreement with values previously determined for rabbit S1 (Iorga *et al.*, 2007).

The values of $1/K_1$, the reciprocal of the equilibrium constant for the formation of the complex actin·S1·ATP, are in the range of 600-1000 μM and roughly independent of temperature as shown by the Van't Hoff plot (ln K_1:1/T) in Fig. 3.2D. In fact the thermodynamic parameters ΔH° and ΔS° estimated with Van't Hoff equation (equation (6)) are not different from zero (Table 2) (Iorga *et al.*, 2007).

3.1.2 ADP affinity of frog S1

Myosin from frog skeletal muscle is thought to have the same kinetic characteristics of the fast myosin isoforms from mammalian skeletal muscle, that have been well characterized in transient kinetics studies (Weiss *et al.*, 2001;

	$\Delta H^{\ddagger}$ (kJ·mol^{-1})	$\Delta S^{\ddagger}$ (J·K^{-1}·mol^{-1})	ΔH° (kJ·mol^{-1})	ΔS° (J·K^{-1}·mol^{-1})
Frog S1	31.9 ± 9.7	167 ± 35	23.6 ± 98.7	-22.44± 27.9

Table 2. Thermodynamic parameters (mean ± SE) of the ATP induced dissociation of pyr·actin-frogS1 estimated using equation (6) (ΔH°, ΔS°) and equation (7) ($\Delta H^{\ddagger}$, $\Delta S^{\ddagger}$).

Nyitrai *et al.*, 2006; Iorga *et al.*, 2007). The most relevant kinetic characteristic of the fast myosin isoforms concerns the ADP release step. In particular fast isoforms have a weaker ADP affinity and a higher rate constant for ADP release than the slower isoforms. Furthermore, in fast isoforms, the ADP is in rapid equilibrium with actin-S1 complex compared with the rate constant of ATP induced actin-S1 dissociation; therefore the ADP acts as a competitive inhibitor of ATP dissociation reaction as described by equation (5). To define the ADP affinity for frog myosin, we have determined the effect of [ADP] on the ATP induced dissociation of actin·S1 complex. In these experiments 500 μM ATP were pre-mixed with different ADP concentrations and then mixed with 1 μM pyr·actin-frogS1.The [ADP] used ranged from 0 to 2000 μM. Fig. 3.3A shows the fluorescence transients obtained using 50 μM, 1 and 2 mM ADP. For all [ADP] the transients are well fitted with a single exponential function and at 5°C k_{obs} is 127 ± 2 s^{-1}, 73.7 ± 1.0 s^{-1} and 31.26 ± 0.26 s^{-1} for 50 μM, 1 and 2 mM ADP concentrations, respectively. Pre mixing the ATP with various concentrations of ADP results in a marked slowing of the observed reaction and k_{obs} shows a hyperbolic dependence on increasing [ADP] (Fig. 3.3B). The hyperbolic fit of the data with equation (5) gave a value for K_{ADP} of 644 ± 71 μM. The high value of K_{ADP} indicates a low ADP affinity as expected for a fast myosin isoforms. In fact K_{ADP} for rat 2X and 2B isoforms is ~550 μM and ~530 μM respectively (Nyitrai *et al.*, 2006).

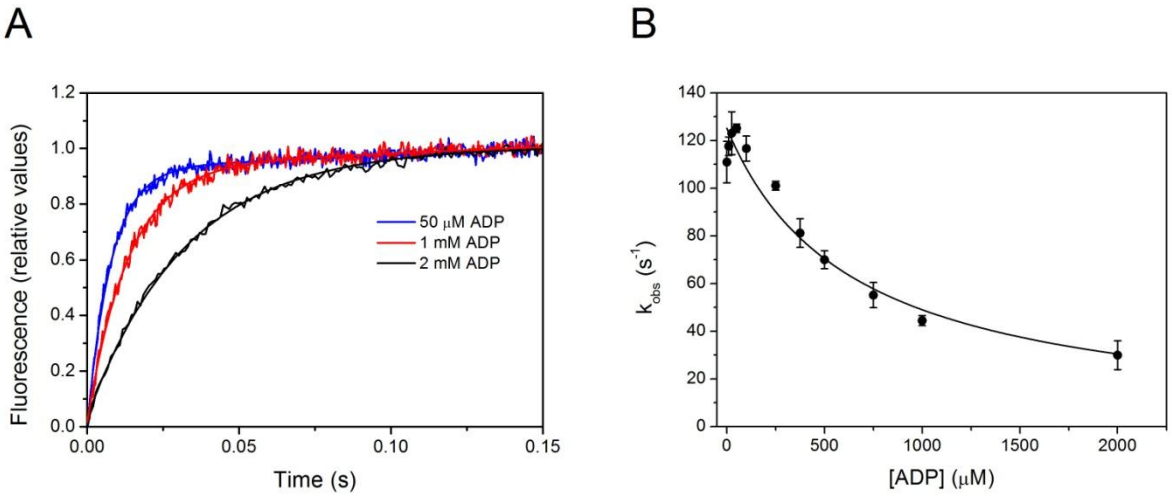

Fig. 3.3. ADP affinity (K_{AD}) of frogS1. **A.** Pyrene fluorescence transient of 1 μM pyr·actin-frogS1 mixed 500 μM ATP preincubated with 50 μM, 1, 2 mM ADP. Continuous lines are the fit of the trace with a single exponential equation. **B.** Plot of k_{obs} as a function of [ADP]. Continuous line is the of the data with equation (5). Experimental conditions:5°C, 100 mM KCl, 20 mM cacodylate pH 7.0, 5 mM $MgCl_2$ and 1 mM NaN_3.

3.2 IVMA experiments on the fragments from frog myosin

3.2.1 V_F in control conditions

For IVMA studies the HMM fragment is the most suitable specimen, as it maintains the dimeric nature of the whole molecule. The sliding velocity (V_F) of actin filaments over a nitrocellulose coated surface carrying HMM from frog skeletal muscle in control conditions is shown in Fig 3.4. V_F, obtained from 86 filaments selected from 4 slides and 2 HMM purifications, was 6.91 ± 0.06 μm·s^{-1}. V_F is about 30% higher than the value obtained using whole myosin molecule under the same conditions (V_F = 5.28 ± 0.09 μm·s^{-1}; Elangovan *et al*., 2012), in agreement with what previously observed for rabbit (Kron & Spudich, 1986; Toyoshima *et al.*, 1987). This is likely related to rise of a drag force when the myosin molecule is used, due to the aspecific interactions between myosin tails and actin filaments (Guo & Guilford, 2004).

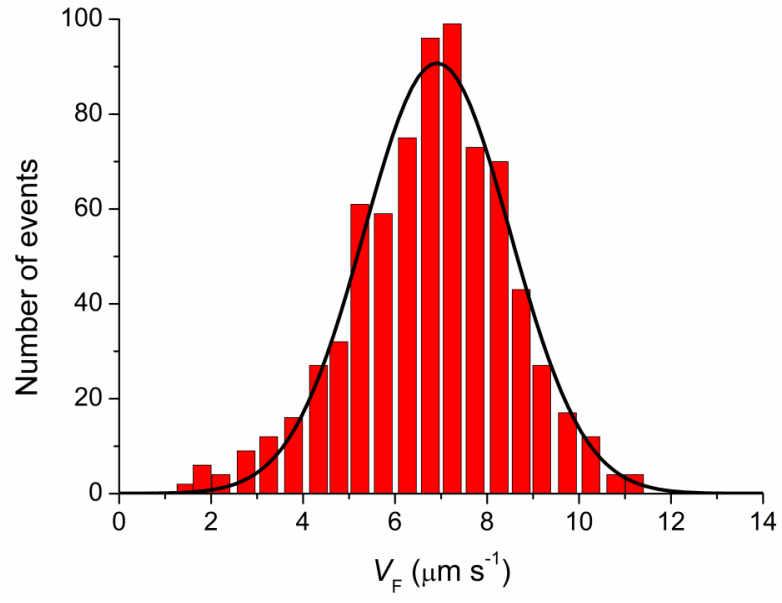

Fig. 3.4. Frequency distribution of the frame to frame velocity of actin filaments (V_F) on HMM fragments from frog skeletal muscle under control conditions. V_F was grouped with bin size of 0.5 μm·s^{-1}. The continuos line is the least-square fit using the gaussian equation (9). Estimated parameters are (mean ± SE): 6.91 ± 0.06 μm·s^{-1}

3.2.2 Effects of HMM concentration

For MYOMAC experiments it is of crucial importance to control the number and spatial frequency of molecular motors interacting with the actin filament. This

can be achieved by maximizing the probability that only one motor protein is deposited on the tip of each pillar that composes the final version of the nanostructured surface. For this purpose it is also important to define the proper motor concentration to be used. In this view, we have determined if and how the HMM concentration affects V_F and what is the minimum HMM concentration required, by incubating for 5 minutes the flow cell with solutions with different HMM concentrations in the range 0.025-0.4 mg·ml^{-1}. Fig. 3.5 shows the relation between V_F and HMM concentration in the incubation solution. In the range of myosin concentrations of 0.2-0.4 mg·ml^{-1}, V_F remained almost constant (average value 4.70 ± 0.06 mg·ml^{-1}) independently of the HMM concentration. This agrees with the results of similar experiments done using the whole myosin molecule from frog muscle (Elangovan *et al.*, 2012). At concentrations below 0.2 mg·ml^{-1}, V_F decreases progressively with the reduction of the [HMM]. With the threshold conditions selected according to the criteria described in Methods, no sliding was observed when the flow cell was incubated with [HMM] below the 0.05 mg·ml^{-1}.

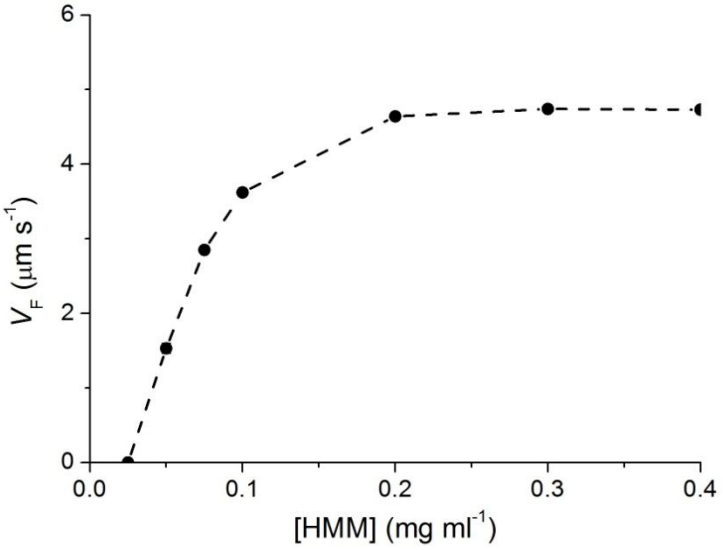

Fig. 3.5. Relation between V_F and frog HMM concentration. V_F was determined in the range of [HMM] 0.025-0.4 mg·ml^{-1}. Each point (mean ± SE from at least 30 filaments) was obtained from the same HMM preparation. The dashed line connects the points for sake of clarity. Experimental conditions: 60 mM ionic strength, 2 mM ATP, pH 7.5 and 20°C.

3.2.3 Effect of temperature

The dependence of V_F on temperature was determined under otherwise control conditions in the range of temperatures between 5 and 25°C. As shown in Fig. 3.6A, in the whole range of temperatures used, the sliding velocity increased with the increase in temperature from 0.691 ± 0.017 µm·s^{-1} at 5°C (2 slides) to 7.80 ± 0.14 µm·s^{-1} at 30°C (2 slides).

To better define the temperature dependence of V_F, the data of Fig. 3.6A are used to build the Arrhenius plot of Fig. 3.6B, where log V_F is plotted versus 1/T (the reciprocal of absolute temperature) according to the equation:

$$\log(V_F) = \log(k) + \frac{E_a}{2.303 \cdot R} \cdot \left(\frac{1}{T}\right) \qquad (10),$$

where E_a is the activation energy, R is the gas constant (8.314 J mol^{-1} K^{-1}). The slope of the relation (E_a/(2.303 x R)) estimates E_a, while the ordinate intercept of the relation (log(k)) is the kinetic prefactor. As previously found for both frog and mammalian myosin (Homsher *et al.*, 2003; Rossi *et al.*, 2005; Elangovan *et al.*, 2012), the slope of the relation, and thus E_a, reduces at higher temperature. Assuming that the change in the slope occurs at ~20°C (1/T ≤ 3.4 x 10^{-3}), E_a was -27.95 ± 5.85 kJ mol^{-1} in the range 20-30°C (dashed line) and -85.01 ± 4.79 kJ mol^{-1} in the range 5-20°C (dotted line). Compared to the values previously determined on frog myosin (Elangovan *et al.*, 2012), E_a is similar in the range of 20-30°C but higher in the range of 5-20°C. In this range, however, E_a is similar to the value found with mammalian HMM and fish myosin (Homsher *et al.*, 2003; Grove *et al.*, 2005; Rossi *et al.*, 2005).

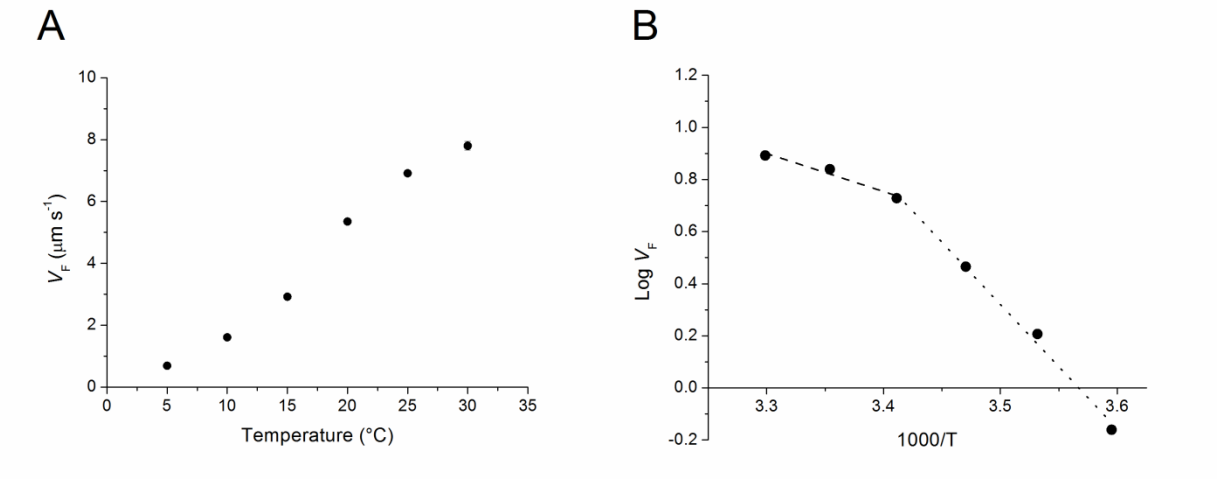

Fig. 3.6. Temperature dependence of V_F on frog HMM. **A.** Relation between V_F and temperature (°C). All points (mean ± SE, from 2 slides and at least 30 filaments) were obtained from the same HMM preparation. **B.** Arrhenius plot of data from A. The dashed line is the linear regression to V_F data for temperatures ≥ 20°C (1/T ≥ 3.4 x 10^{-3}), the parameters estimated by the fit are: slope -1.46 ± 0.29, intercept 5.71 ± 0.96; the dotted line is the linear regression to V_F data for temperatures ≤ 20°C (1/T ≤ 3.4 x 10^{-3}), the parameters estimated by the fit are: slope -4.78 ± 0.25, intercept 17.03 ± 0.88.

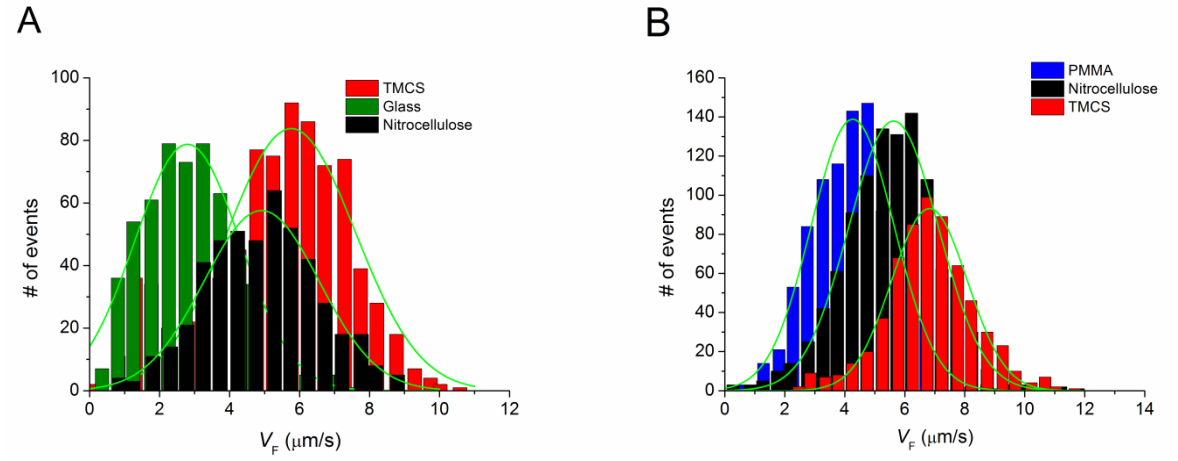

Fig. 3.7. Comparison of V_F for both myosin and HMM from frog skeletal muscle adsorbed on different substrates. **A.** Frequency distribution of V_F on myosin adsorbed on glass (green), nitrocellulose (black) and TMCS (red). The data come from the same myosin preparation; **B.** Frequency distribution of V_F on HMM adsorbed on PMMA (blue), nitrocellulose (black) and TMCS (red). Since no actin movement was observed on HMM adsorbed directly on glass surface, PMMA was chosen as a third substrate. The data come from the same HMM preparation. The continuos lines are the fit to the data with equation (9). V_F estimated by the fits are reported in table 3. Experimental conditions: 20°C, ionic strength 60 mM and pH 7.4.

3.2.4 IVMA on different substrates

The results obtained with the classical surface functionalization with nitrocellulose are compared to those obtained with other kinds of coatings, PMMA and TMCS, to select the best substratum for the myosin motors in relation to the ability to move the actin filament. As shown in Fig 3.7A (for myosin) and B (for HMM) and summarized in table 3, the highest values of V_F were observed when the surface was functionalized with TMCS. V_F is ~20% higher on TMCS than on nitrocellulose for both myosin and HMM. These results are in agreement with those reported for HMM from mammalian skeletal muscle (Sundberg *et al.*, 2003; Albet-Torres *et al.*, 2007).

	Glass	PMMA	Nitrocellulose	TMCS
Myosin V_F (μm·s^{-1}; mean ± SE)	2.79 ± 0.07*		4.92 ± 0.08	5.76 ± 0.14*
HMM V_F (μm·s^{-1}; mean ± SE)		4.26 ± 0.06*	5.63 ± 0.04	6.82 ± 0.04*

Table 3. Values of V_F for both myosin and HMM from frog skeletal muscle adsorbed on different substrates.

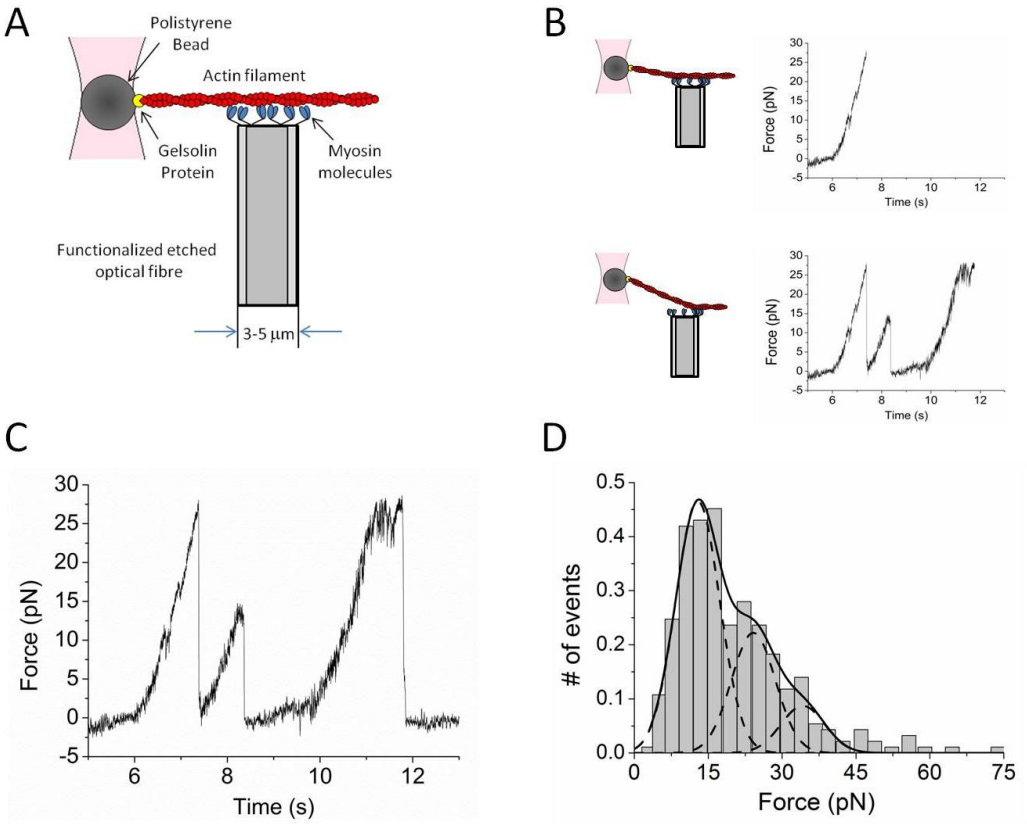

Fig. 3.8. Single unbinding events of frog HMM. **A.** Schematic representation of the experimental protocol arrangement. Frog HMM (0.4 mg·ml^{-1}) are randomly dispersed on the tip of the fibre (grey) functionalized with nitrocellulose. The actin filament is attached to the polystyrene bead (dark grey) by gelsolin protein (yellow). The pink shadow schematically represents the DLOT used to trap the BTA; **B.** Representation of the mechanical protocol consisting in the movement of the motor support away from the actin filament in the perpendicular direction **C.** Force trace of three unbinding events of frog HMM obtained pulling the fibre at the velocity 1 μm/s. **D.** Frequency distribution of the rupture force. Continuous line: three-Gaussian fit to the data with σ constrained to be the same. Dashed line: Single Gaussian functions reconstructed using the parameters obtained fitting the data with three-Gaussian function. Estimated parameters: C_1: 12.85 ± 0.35, C_2: 24.16 ± 1.15, C_3: 34.21 ± 2.01 and σ: 8.94 ± 0.59. Experimental conditions: 20°C, 60 mM ionic strength and pH 7.4.

3.3 Mechanical measurements on a limited ensemble of myosin motors

3.3.1 Rupture force of the actin-HMM complex in ATP free solution

The first mechanical measurements have been done using the DLOT on a simplified version of the MYOMAC assay. In this version HMM are randomly dispersed on the flat tip of an etched optical fibre (3-8 μm in diameter, Fig. 3.8A). In this way the number of myosin motors interacting with the actin filament is

limited by the dimensions of the etched optical fibre. Binding-unbinding events between the motor proteins and the bead tailed actin filament in ATP-free solution were observed by moving (1 $\mu m \cdot s^{-1}$) the myosin motor covered surface perpendicular to the actin filament (Fig. 3.8B).

Fig. 3.8C shows the time course of force for three unbinding events, identified by the rapid drop of force. The frequency distribution of the force of unbinding events is shown in Fig. 3.8D. The distribution can be fitted by three Gaussians with the same sigma (σ: 8.94 ± 0.59 pN) and centre at 12.85 ± 0.35 pN, 24.16 ± 1.15 pN and 34.21 ± 2.01 pN. The rupture force distributes in a range of forces 7-50 pN with frequency peaking at forces multiple of ~13 pN.

Chapter 4 – DISCUSSION

This thesis reports the achievements towards the realization of a synthetic sarcomere like machine (MYOMAC), consisting in the interaction of an actin filament with an array of myosin motors carried on a nanostructured surface.

The main goals reached in this research are: (*i*) Preparation of the myosin motors from frog skeletal muscle (both myosin molecule and proteolytic fragments); (*ii*) test on the kinetic and mechanical properties of the motors with transient kinetic techniques and *In vitro* motility assay; (*iii*) attachment of the barbed end of the actin filament to a bead, to control the correct polarity of the actin filament in the machine; (*iv*) realization of a flow chamber with several compartments so that the elements of the machine are brought into contact in a controlled way; (*v*) mechanical measurements of the interactions between the actin filament and the motor array in a simplified version of MYOMAC in which the support for the motors is provided by the flat tip of an etched optical fibre; (*vi*) measurement of the rupture force of a single actin-myosin bond in ATP free solution.

4.1 Kinetic properties of myosin motors in solution

The muscle myosin selected for the machine is extracted from the skeletal muscle of the frog, the species that has provided the standard mechanical and energetic parameters of myosin motors *in situ* (Woledge *et al*., 1985). However, no definitive data are present in literature about the kinetic properties of frog myosin especially as regards its proteolytic fragments that are the preferred preparation for the machine. Transient kinetic techniques are applied for the first time to S1 from frog skeletal muscle to determine: (*i*) the dissociation of actin-S1complex by ATP and its temperature dependence and (*ii*) the affinity of S1 for ADP. As expected for a fast myosin isoform, frog S1 showed a fast monophasic actin-myosin dissociation by ATP (k_{+2} ~500·s^{-1}, 1/K_1 ~850 μM at 5°C) (Fig. 3.1) and a low ADP affinity (K_{ADP} ~650 μM at 5°C) (Fig. 3.3). Moreover, the maximum

dissociation rate constant k_{+2} increased from ~500 s^{-1} at 5°C to ~850 s^{-1} at 15°C (Figs 3.2B and C). Both the activation enthalpy ($\Delta H^{\ddagger}$ ~32 $kJ \cdot mol^{-1}$) and activation entropy ($\Delta S^{\ddagger}$ ~170 $J \cdot K^{-1} \cdot mol^{-1}$) estimated with the Arrhenius plot of k_{+2}, were positive and in agreement with the values previously estimated for rabbit S1 (Siemankowski *et al.*, 1985; Iorga *et al.*, 2007). Conversely, the equilibrium constant for the complex formation was almost independent of temperature (Fig 3.2 B and D) and the thermodynamic parameters $\Delta H°$ and $\Delta S°$ were not statistically different from zero.

The kinetics of the two biochemical steps in solution measured above should be related to the kinetics of myosin during unloaded shortening of a muscle fibre. The rate constant for the dissociation of ADP from acto-S1 complex (k_{-ADP}) can be calculated assuming a second order rate constant for ADP binding to acto-S1 complex (k_{+ADP}) of 10^7 $M^{-1} \cdot s^{-1}$, the minimum value for a diffusion limited step (Siemankowski & White, 1984; Iorga *et al.*, 2007) and knowing K_{ADP} (~650 μM). The value of k_{-ADP} for frog myosin is ($K_{ADP} \cdot k_{+ADP}$=) 6500 s^{-1}. In a fibre shortening at V_0, k_{min}, the minimum value of the rate constant that limits the shortening velocity, can be easily calculated using equation (2). In single fibre from frog skeletal muscle at 5°C V_0=~2.5 $\mu m \cdot s^{-1}$ and d=~7 nm (Piazzesi *et al.*, 2003; Piazzesi *et al.*, 2007), and therefore k_{min} ~350 s^{-1}. Thus the value of k_{-ADP} from transient kinetics is ~20 times higher than the k_{min} from fibre measurements, demonstrating that the ADP release step cannot be rate-limiting at V_0. Consequently the rate limiting step must be a subsequent step in the ATPase cycle, that is the isomerization step that follows the ATP binding and leads to dissociation. Actually k_{+2}, the rate constant for this step measured in solution from frog S1 is 500 s^{-1}, in good agreement with k_{min} (350 s^{-1}) value calculated from fibre measurements at V_0.

The value of k_{-ADP} calculated in this work is also ~20 times higher than the value estimated in IVMA experiments on frog myosin II (Elangovan *et al.*, 2012). In fact the ordinate intercept of the relation of d/V_F versus 1/[ATP] in Fig. 9 of Elangovan *et al.* (~300 s^{-1}) should correspond to the rate of ADP dissociation according to the equation (8) in Elangovan *et al.*:

$$\frac{d}{V_F} = \frac{1}{k_{-ADP}} + \frac{1}{[\mathrm{ATP}] \cdot k_{+ATP}}$$

The contradiction derives from the fact that in that work the ATP induced dissociation of the actin-myosin complex is considered to occur as a single step.

According to our solution kinetic studies and scheme 1, this is an oversimplification of the reaction and the ordinate intercept of d/V_F:1/[ATP] relation in IVMA experiments depends on whatever is the rate limiting step at saturating ATP, likely the isomerization step. Indeed, the value found by Elangovan *et al.* is in good agreement with the value of k_{+2} measured in this thesis.

4.2 IVMA with frog myosin fragments

For the first time the HMM fragments prepared from frog skeletal muscle have been successfully used in IVMA experiments. Frog HMM shows a long lasting capability to propel the actin filaments and in almost all the experiments the actin filaments move continuously and smoothly.

V_F measured in control condition on frog HMM is 6.91 ± 0.06 $\mu m \cdot s^{-1}$ and is ~20% higher than the value obtained using whole myosin II molecule (Elangovan *et al.*, 2012). Since the only difference is the presence of the tail in whole myosin molecule, the lower value of V_F is likely due to the load generated by aspecific interactions between the tail of the myosin molecule and the actin filaments. In support to this hypothesis it has been found that addition of LMM to the experimental solution slows down the sliding velocity of actin filaments in IVMA with rat HMM (Guo & Guilford, 2004).

The difference in V_F between HMM and whole myosin II remains also when the motor proteins are adsorbed on different substrates. Nitrocellulose, TMCS-derivatized surfaces and PMMA/glass have been used as myosin motor adsorbing surfaces to establish the best substrate to be used in MYOMAC experiments. For all substrates, V_F with HMM was 15-20% higher than with whole myosin II (Fig. 3.7). Moreover, as already observed for mammalian myosin (Sundberg *et al.*, 2003; Albet-Torres *et al.*, 2007), the highest value of V_F was observed on TMCS-derivatized surface.

The effect of temperature on V_F has been measured in the range of temperatures 5-30°C (Fig. 3.6A). In the whole range, V_F increased with increase in temperature, however, as already observed for mammalian myosin isoforms (Rossi et al., 2005) and frog myosin II (Elangovan *et al.*, 2012), the temperature sensitivity of V_F of frog HMM is higher in the lower temperature range (5-20°C) (Fig. 3.6B). The lower sensitivity at temperatures beyond 20°C is not due to denaturation of the myosin or to a change in the pH of the solutions since (*i*) the

effect of temperature on V_F has been found to be fully reversible; (*ii*) the pH of all solutions is adjusted at the final experimental temperature. Therefore, as already suggested for mammalian myosin (Rossi *et al.*, 2005), the change in temperature sensitivity could be due to a change in the catalytic activity of the molecule or in the step of ATPase cycle that limits V_F.

4.3 Rupture force of actin-HMM bond in ATP free solution

A simplified version of MYOMAC, where the motor proteins are randomly dispersed on the flat tip of an etched optical fibre, has been used to measure the force of unbinding events between frog HMM and actin filament. The rupture forces are distributed in a range of values 7-50 pN. The frequency histogram can be fitted with three Gaussians with the same σ (9 pN) and centre at 13 pN, 24 pN and 34 pN (Fig. 3.8D). This indicates that rupture forces of amplitude ~13 pN can occur either as single events or in clusters of two or three events. Therefore, up to three bonds at maximum can be formed in a relatively small region of the actin filament as a consequence of the clustering of HMM on the tip of glass fibre. A rupture force of 13 pN is in agreement with previous measurements on rabbit HMM (~9 pN, (Nishizaka *et al.*, 1995)) and rat HMM (~15 pN, (Guo & Guilford, 2006)) using single beam optical tweezers.

A multi-peak distribution of rupture forces has also been found for the unbinding events of actin-HMM using Atomic Force Microscopy (AFM) technique (Nakajima *et al.*, 1997) and a streptavidin coated bead to attach, on one side, the biotynilated tail of rabbit HMM and, on the other, the biotynilated tip of the AFM cantilever. The rupture forces in that work distribute around two force regions centered at 14.8 pN and 24.7 pN, similar to the first two peaks of the rupture force distribution observed in this work.

The comparison of our data with previous measurements demonstrates the power and the reliability of the method under development for the mechanics of the MYOMAC. In fact (*i*) the DLOT expands the dynamic range of force (up to 200 pN), to make it adequate to record forces from an array of myosin motors, overcoming the force limits imposed by single laser trap methods; (*ii*) the method of attaching the actin filament to the bead via gelsolin ensures the right polarity for

the interaction of actin with the motor array and at the same time the adequate strength of the actin-bead link for the range of forces developed by a motor array.

Bibliography

1. Adamek N, Coluccio LM & Geeves MA (2008). Calcium sensitivity of the cross-bridge cycle of Myo1c, the adaptation motor in the inner ear. *Proc Natl Acad Sci USA* **105,** 5710-5715.

2. Albet-Torres N, Gunnarsson A, Persson M, Balaz M, Hook F & Mansson A (2010). Molecular motors on lipid bilayers and silicon dioxide: different driving forces for adsorption. *Soft Matter* **6,** 3211-3219.

3. Albet-Torres N, O'mahony J, Charlton C, Balaz M, Lisboa P, Aastrup T, Mansson A & Nicholls IA (2007). Mode of heavy meromyosin adsorption and motor function correlated with surface hydrophobicity and charge. *Langmuir* **23,** 11147-11156.

4. Allen PG (2003). Actin filament uncapping localizes to ruffling lamellae and rocketing vesicles. *Nat Cell Biol* **5,** 972-979.

5. Ashkin A (1970). Acceleration and trapping of particles by radiation pressure. *Phys Rev Lett* **24,** 156-159.

6. Ashkin A (1992). Forces of a single-beam gradient laser trap on a dielectric sphere in the ray optics regime. *Biophys J* **61,** 569-582.

7. Ashkin A & Dziedzic JM (1987). Optical trapping and manipulation of viruses and bacteria. *Science* **235,** 1517-1520.

8. Ashkin A & Dziedzic JM (1989). Internal cell manipulation using infrared laser traps. *Proc Natl Acad Sci USA* **86,** 7914-7918.

9. Ashkin A, Dziedzic JM, Bjorkholm JE & Chu S (1986). Observation of a single-beam gradient force optical trap for dielectric particles. *Opt Lett* **11,** 288-290.

10. Ashkin A, Dziedzic JM & Yamane T (1987). Optical trapping and manipulation of single cells using infrared laser beams. *Nature* **330,** 769-771.

11. Barclay CJ, Constable JK & Gibbs CL (1993). Energetics of fast- and slow-twitch muscles of the mouse. *J Physiol* **472,** 61-80.

12. Bianco P, Bongini L, Melli L, Dolfi M & Lombardi V (2011). Piconewton-millisecond force steps reveal the transition kinetics and mechanism of the double-stranded DNA elongation. *Biophys J* **101,** 866-874.

13. Binnig G, Quate CF & Gerber C (1986). Atomic force microscope. *Phys Rev Lett* **56,** 930.

14. Bloemink MJ, Adamek N, Reggiani C & Geeves MA (2007). Kinetic analysis of the slow skeletal myosin MHC-1 isoform from bovine masseter muscle. *J Mol Biol* **373,** 1184-1197.

15. Bloemink MJ, Melkani GC, Dambacher CM, Bernstein SI & Geeves MA (2011). Two Drosophila myosin transducer mutants with distinct cardiomyopathies have divergent ADP and actin affinities. *J Biol Chem* **286,** 28435-28443.

16. Brunello E, Reconditi M, Elangovan R, Linari M, Sun YB, Narayanan T, Panine P, Piazzesi G, Irving M & Lombardi V (2007). Skeletal muscle resists stretch by rapid binding of the second motor domain of myosin to actin. *Proc Natl Acad Sci USA* **104,** 20114-20119.

17. Bunk R, Klinth J, Montelius L, Nicholls IA, Omling P, Tagerud S & Mansson A (2003). Actomyosin motility on nanostructured surfaces. *Biochem Biophys Res Commun* **301,** 783-788.

18. Canepari M, Maffei M, Longa E, Geeves M & Bottinelli R (2012). Actomyosin kinetics of pure fast and slow rat myosin isoforms studied by *in vitro* motility assay approach. *Exp Physiol* **97,** 873-881.

19. Canepari M, Rossi R, Pellegrino MA, Reggiani C & Bottinelli R (1999). Speeds of actin translocation *in vitro* by myosins extracted from single rat muscle fibres of different types. *Exp Physiol* **84,** 803-806.

20. Capitanio M, Canepari M, Cacciafesta P, Lombardi V, Cicchi R, Maffei M, Pavone FS & Bottinelli R (2006). Two independent mechanical events in the interaction cycle of skeletal muscle myosin with actin. *Proc Natl Acad Sci USA* **103,** 87-92.

21. Capitanio M, Canepari M, Maffei M, Beneventi D, Monico C, Vanzi F, Bottinelli R & Pavone FS (2012). Ultrafast force-clamp spectroscopy of single molecules reveals load dependence of myosin working stroke. *Nat Meth* **9,** 1013-1019.

22. Caremani M, Dantzig J, Goldman YE, Lombardi V & Linari M (2008). Effect of inorganic phosphate on the force and number of myosin cross-bridges during the isometric contraction of permeabilized muscle fibers from rabbit psoas. *Biophys J* **95,** 5798-5808.

23. Chaponnier C, Janmey PA & Yin HL (1986). The actin filament-severing domain of plasma gelsolin. *J Cell Biol* **103,** 1473-1481.

24. Choe H, Burtnick LD, Mejillano M, Yin HL, Robinson RC & Choe S (2002). The calcium activation of gelsolin: Insights from the 3Å structure of the G4–G6/actin complex. *J Mol Biol* **324,** 691-702.

25. Cluzel P, Lebrun A, Heller C, Lavery R, Viovy JL, Chatenay D & Caron F (1996). DNA: an extensible molecule. *Science* **271,** 792-794.

26. Coluccio LM & Geeves MA (1999). Transient kinetic analysis of the 130-kDa myosin I (MYR-1 Gene Product) from rat liver: A MYOSIN I DESIGNED FOR MAINTENANCE OF TENSION? *J Biol Chem* **274,** 21575-21580.

27. Criddle AH, Geeves MA & Jeffries T (1985). The use of actin labelled with N-(1-pyrenyl)iodoacetamide to study the interaction of actin with myosin subfragments and troponin/tropomyosin. *Biochem J* **232,** 343-349.

28. Denk W & Webb WW (1990). Optical measurement of picometer displacements of transparent microscopic objects. *Appl Opt* **29,** 2382-2391.

29. Dos Remedios CG, Chhabra D, Kekic M, Dedova IV, Tsubakihara M, Berry DA & Nosworthy NJ (2003). Actin binding proteins: Regulation of cytoskeletal microfilaments. *Physiol Rev* **83,** 433-473.

30. Elangovan R, Capitanio M, Melli L, Pavone FS, Lombardi V & Piazzesi G (2012). An integrated *in vitro* and *in situ* study of kinetics of myosin II from frog skeletal muscle. *J Physiol* **590,** 1227-1242.

31. Essevaz-Roulet B, Bockelmann U & Heslot F (1997). Mechanical separation of the complementary strands of DNA. *Proc Natl Acad Sci USA* **94,** 11935-11940.

32. Fenn WO (1924). The relation between the work performed and the energy liberated in muscular contraction. *J Physiol* **58,** 373.

33. Ferenczi MA, Homsher E, Simmons RM & Trentham DR (1978a). Reaction mechanism of the magnesium ion-dependent adenosine triphosphatase of frog muscle myosin and subfragment 1. *Biochem J* **171,** 165-175.

34. Ferenczi MA, Homsher E, Trentham DR & Weeds AG (1978b). Preparation and characterization of frog muscle myosin subfragment 1 and actin. *Biochem J* **171,** 155-163.

35. Ferrer JM, Lee H, Chen J, Pelz B, Nakamura F, Kamm RD & Lang MJ (2008). Measuring molecular rupture forces between single actin filaments and actin-binding proteins. *Proc Natl Acad Sci USA* **105,** 9221-9226.

36. Finer JT, Mehta AD & Spudich JA (1995). Characterization of single actin-myosin interactions. *Biophys J* **68,** 291-296.

37. Finer JT, Simmons RM & Spudich JA (1994). Single myosin molecule mechanics: piconewton forces and nanometre steps. *Nature* **368,** 113-119.

38. Geeves MA & Holmes KC (2005). The molecular mechanism of muscle contraction. *Adv Protein Chem* **71,** 161-193.

39. Geeves MA, Jeffries TE & Millar NC (1986). ATP-induced dissociation of rabbit skeletal actomyosin subfragment 1. Characterization of an isomerization of the ternary acto-S1-ATP complex. *Biochemistry* **25,** 8454-8458.

40. Ghislain LP, Switz NA & Webb WW (1994). Measurement of small forces using an optical trap. *Rev Sci Instrum* **65,** 2762-2768.

41. Goldman YE, Hibberd MG, Mc Cray JA & Trentham DR (1982). Relaxation of muscle fibres by photolysis of caged ATP. *Nature* **300,** 701-705.

42. Gremm D & Wegner A (2000). Gelsolin as a calcium-regulated actin filament-capping protein. *Eur J Biochem* **267,** 4339-4345.

43. Grove TJ, Mc Fadden LA, Chase PB & Moerland TS (2005). Effects of temperature, ionic strength and pH on the function of skeletal muscle myosin from a eurythermal fish, *Fundulus heteroclitus*. *J Muscle Res Cell Motil* **26,** 191-197.

44. Guo B & Guilford WH (2004). The tail of myosin reduces actin filament velocity in the *in vitro* motility assay. *Cell Motil Cytoskeleton* **59,** 264-272.

45. Guo B & Guilford WH (2006). Mechanics of actomyosin bonds in different nucleotide states are tuned to muscle contraction. *Proc Natl Acad Sci USA* **103,** 9844-9849.

46. Hellam DC & Podolsky RJ (1969). Force measurements in skinned muscle fibres. *J Physiol* **200,** 807-819.

47. Hill AV (1938). The heat of shortening and the dynamic constants of muscle. *Proc R Soc Lond B Biol Sci* **126,** 136-195.

48. Holmes KC, Popp D, Gebhard W & Kabsch W (1990). Atomic model of the actin filament. *Nature* **347,** 44-49.

49. Holmes KC, Tirion M, Popp D, Lorenz M, Kabsch W & Milligan RA (1993). A comparison of the atomic model of F-actin with cryo-electron micrographs of actin and decorated actin. *Adv Exp Med Biol* **332,** 15-22.

50. Homsher E, Nili M, Chen IY & Tobacman LS (2003). Regulatory proteins alter nucleotide binding to acto-myosin of sliding filaments in motility assays. *Biophys J* **85,** 1046-1052.

51. Homsher E, Wang F & Sellers JR (1992). Factors affecting movement of F-actin filaments propelled by skeletal muscle heavy meromyosin. *Am J Physiol* **262,** 714-723.

52. Howard J & Hyman AA (1993). Chapter 7. Preparation of marked microtubules for the assay of the polarity of microtubule-based motors by fluorescence microscopy. In *Methods Cell Biol*, ed. Jonathan MS, pp 105-113. Academic Press.

53. Huxley AF (1957). Muscle structure and theories of contraction. *Prog Biophys Biophys Chem* **7,** 255-318.

54. Huxley AF & Niedergerke R (1954). Structural changes in muscle during contraction; interference microscopy of living muscle fibres. *Nature* **173,** 971-973.

55. Huxley HE (1969). The mechanism of muscular contraction. *Science* **164,** 1356-1365.

56. Huxley HE & Hanson J (1954). Changes in the cross-striations of muscle during contraction and stretch and their structural interpretation. *Nature* **173,** 973-976.

57. Hwo S & Bryan J (1986). Immuno-identification of Ca^{2+}-induced conformational changes in human gelsolin and brevin. *J Cell Biol* **102,** 227-236.

58. Iorga B, Adamek N & Geeves MA (2007). The slow skeletal muscle isoform of myosin shows kinetic features common to smooth and non-muscle myosins. *J Biol Chem* **282,** 3559-3570.

59. Ishijima A, Doi T, Sakurada K & Yanagida T (1991). Sub-piconewton force fluctuations of actomyosin *in vitro*. *Nature* **352,** 301-306.

60. Janmey PA, Iida K, Yin HL & Stossel TP (1987). Polyphosphoinositide micelles and polyphosphoinositide-containing vesicles dissociate endogenous gelsolin-actin

complexes and promote actin assembly from the fast-growing end of actin filaments blocked by gelsolin. *J Biol Chem* **262,** 12228-12236.

61. Janmey PA & Stossel TP (1987). Modulation of gelsolin function by phosphatidylinositol 4,5-bisphosphate. *Nature* **325,** 362-364.

62. Kabsch W, Mannherz HG, Suck D, Pai EF & Holmes KC (1990). Atomic structure of the actin:DNase I complex. *Nature* **347,** 37-44.

63. Kishino A & Yanagida T (1988). Force measurements by micromanipulation of a single actin filament by glass needles. *Nature* **334,** 74-76.

64. Kothakota S, Azuma T, Reinhard C, Klippel A, Tang J, Chu K, Mc Garry TJ, Kirschner MW, Koths K, Kwiatkowski DJ & Williams LT (1997). Caspase-3-generated fragment of gelsolin: Effector of morphological change in apoptosis. *Science* **278,** 294-298.

65. Kron SJ & Spudich JA (1986). Fluorescent actin filaments move on myosin fixed to a glass surface. *Proc Natl Acad Sci USA* **83,** 6272-6276.

66. Kron SJ, Toyoshima YY, Uyeda TQ & Spudich JA (1991). Assays for actin sliding movement over myosin-coated surfaces. *Methods Enzymol* **196,** 399-416.

67. Kushmerick MJ, Larson RE & Davies RE (1969). The chemical energetics of muscle contraction. I. Activation heat, heat of shortening and ATP utilization for activation-relaxation processes. *Proc R Soc Lond B Biol Sci* **174,** 293-313.

68. Kwiatkowski DJ, Janmey PA, Mole JE & Yin HL (1985). Isolation and properties of two actin-binding domains in gelsolin. *J Biol Chem* **260,** 15232-15238.

69. Kwiatkowski DJ, Janmey PA & Yin HL (1989). Identification of critical functional and regulatory domains in gelsolin. *J Cell Biol* **108,** 1717-1726.

70. Kwiatkowski DJ, Stossel TP, Orkin SH, Mole JE, Coltens HR & Yin HL (1986). Plasma and cytoplasmic gelsolins are encoded by a single gene and contain a duplicated actin-binding domain. *Nature* **323,** 455-458.

71. Lee GU, Chrisey LA & Colton RJ (1994). Direct measurement of the forces between complementary strands of DNA. *Science* **266,** 771-773.

72. Lowey S, Waller GS & Trybus KM (1993). Function of skeletal muscle myosin heavy and light chain isoforms by an *in vitro* motility assay. *J Biol Chem* **268,** 20414-20418.

73. Lymn RW & Taylor EW (1971). Mechanism of adenosine triphosphate hydrolysis by actomyosin. *Biochemistry* **10,** 4617-4624.

74. Mansson A, Balaz M, Albet-Torres N & Rosengren KJ (2008). *In vitro* assays of molecular motors-impact of motor-surface interactions. *Front Biosci* **13,** 5732-5754.

75. Millar NC & Geeves MA (1983). The limiting rate of the ATP-mediated dissociation of actin from rabbit skeletal muscle myosin subfragment 1. *FEBS Lett* **160,** 141-148.

76. Miyata H, Yasuda R & Kinosita K, Jr. (1996). Strength and lifetime of the bond between actin and skeletal muscle α-actinin studied with an optical trapping technique. *Biochim Biophys Acta-Gen Subj* **1290,** 83-88.

77. Molloy JE, Burns JE, Kendrick-Jones J, Tregear RT & White DC (1995). Movement and force produced by a single myosin head. *Nature* **378,** 209-212.

78. Murphy CT, Rock RS & Spudich JA (2001). A myosin II mutation uncouples ATPase activity from motility and shortens step size. *Nat Cell Biol* **3,** 311-315.

79. Nakajima H, Kunioka Y, Nakano K, Shimizu K, Seto M & Ando T (1997). Scanning Force Microscopy of the Interaction Events between a Single Molecule of Heavy Meromyosin and Actin. *Biochem Biophys Res Commun* **234,** 178-182.

80. Nishizaka T, Miyata H, Yoshikawa H, Ishiwata SI & Kinosita K, Jr. (1995). Unbinding force of a single motor molecule of muscle measured using optical tweezers. *Nature* **377,** 251-254.

81. Nishizaka T, Seo R, Tadakuma H, Kinosita K, Jr. & Ishiwata S (2000). Characterization of single actomyosin rigor bonds: load dependence of lifetime and mechanical properties. *Biophys J* **79,** 962-974.

82. Nyitrai M & Geeves MA (2004). Adenosine diphosphate and strain sensitivity in myosin motors. *Philos Trans R Soc Lond B Biol Sci* **359,** 1867-1877.

83. Nyitrai M, Rossi R, Adamek N, Pellegrino MA, Bottinelli R & Geeves MA (2006). What limits the velocity of fast-skeletal muscle contraction in mammals? *J Mol Biol* **355,** 432-442.

84. Pantaloni D & Carlier MF (1993). How profilin promotes actin filament assembly in the presence of thymosin β4. *Cell* **75,** 1007-1014.

85. Pardee JD & Spudich JA (1982). Purification of muscle actin. *Methods Enzymol* **85** 164-181.

86. Perelroizen I, Didry D, Christensen H, Chua NH & Carlier MF (1996). Role of nucleotide exchange and hydrolysis in the function of profilin in actin assembly. *J Biol Chem* **271,** 12302-12309.

87. Persson M, Albet-Torres N, Ionov L, Sundberg M, Hook F, Diez S, Mansson A & Balaz M (2010). Heavy meromyosin molecules extending more than 50 nm above adsorbing electronegative surfaces. *Langmuir* **26,** 9927-9936.

88. Piazzesi G, Reconditi M, Koubassova N, Decostre V, Linari M, Lucii L & Lombardi V (2003). Temperature dependence of the force-generating process in single fibres from frog skeletal muscle. *J Physiol* **549,** 93-106.

89. Piazzesi G, Reconditi M, Linari M, Lucii L, Bianco P, Brunello E, Decostre V, Stewart A, Gore DB, Irving TC, Irving M & Lombardi V (2007). Skeletal muscle performance determined by modulation of number of myosin motors rather than motor force or stroke size. *Cell* **131,** 784-795.

90. Pope B, Way M & Weeds AG (1991). Two of the three actin-binding domains of gelsolin bind to the same subdomain of actin implications for capping and severing mechanisms. *FEBS Lett* **280,** 70-74.

91. Rayment I, Holden HM, Whittaker M, Yohn CB, Lorenz M, Holmes KC & Milligan RA (1993a). Structure of the actin-myosin complex and its implications for muscle contraction. *Science* **261,** 58-65.

92. Rayment I, Rypniewski WR, Schmidt-Base K, Smith R, Tomchick DR, Benning MM, Winkelmann DA, Wesenberg G & Holden HM (1993b). Three-dimensional structure of myosin subfragment-1: a molecular motor. *Science* **261,** 50-58.

93. Rossi R, Maffei M, Bottinelli R & Canepari M (2005). Temperature dependence of speed of actin filaments propelled by slow and fast skeletal myosin isoforms. *J Appl Physiol* **99,** 2239-2245.

94. Sase I, Miyata H, Ishiwata SI & Kinosita K, Jr. (1997). Axial rotation of sliding actin filaments revealed by single-fluorophore imaging. *Proc Natl Acad Sci USA* **94,** 5646-5650.

95. Schiaffino S & Reggiani C (1996). Molecular diversity of myofibrillar proteins: gene regulation and functional significance. *Physiol Rev* **76,** 371-423.

96. Seiler SH, Fischman DA & Leinwand LA (1996). Modulation of myosin filament organization by C-protein family members. *Mol Biol Cell* **7,** 113-127.

97. Sheetz MP & Spudich JA (1983). Movement of myosin-coated fluorescent beads on actin cables *in vitro*. *Nature* **303,** 31-35.

98. Siemankowski RF & White HD (1984). Kinetics of the interaction between actin, ADP, and cardiac myosin-S1. *J Biol Chem* **259,** 5045-5053.

99. Siemankowski RF, Wiseman MO & White HD (1985). ADP dissociation from actomyosin subfragment 1 is sufficiently slow to limit the unloaded shortening velocity in vertebrate muscle. *Proc Natl Acad Sci USA* **82,** 658-662.

100. Smith SB, Cui Y & Bustamante C (1996). Overstretching B-DNA: the elastic response of individual double-stranded and single-stranded DNA molecules. *Science* **271,** 795-799.

101. Smith SB, Cui Y & Bustamante C (2003). Optical-trap force transducer that operates by direct measurement of light momentum. *Methods Enzymol* **361,** 134-162.

102. Spudich JA, Kron SJ & Sheetz MP (1985). Movement of myosin-coated beads on oriented filaments reconstituted from purified actin. *Nature* **315,** 584-586.

103. Sundberg M, Rosengren JP, Bunk R, Lindahl J, Nicholls IA, Tagerud S, Omling P, Montelius L & Mansson A (2003). Silanized surfaces for *in vitro* studies of actomyosin function and nanotechnology applications. *Anal Biochem* **323,** 127-138.

104. Suzuki N, Miyata H, Ishiwata S & Kinosita K, Jr. (1996). Preparation of bead-tailed actin filaments: estimation of the torque produced by the sliding force in an *in vitro* motility assay. *Biophys J* **70,** 401-408.

105. Svoboda K & Block SM (1994). Force and velocity measured for single kinesin molecules. *Cell* **77,** 773-784.

106. Svoboda K, Schmidt CF, Schnapp BJ & Block SM (1993). Direct observation of kinesin stepping by optical trapping interferometry. *Nature* **365,** 721-727.

107. Taft MH, Hartmann FK, Rump A, Keller H, Chizhov I, Manstein DJ & Tsiavaliaris G (2008). Dictyostelium myosin-5b is a conditional processive motor. *J Biol Chem* **283,** 26902-26910.

108. Tanaka H, Ishijima A, Honda M, Saito K & Yanagida T (1998). Orientation dependence of displacements by a single one-headed myosin relative to the actin filament. *Biophys J* **75,** 1886-1894.

109. Toyoshima YY, Kron SJ, Mcnally EM, Niebling KR, Toyoshima C & Spudich JA (1987). Myosin subfragment-1 is sufficient to move actin filaments *in vitro*. *Nature* **328,** 536-539.

110. Toyoshima YY, Toyoshima C & Spudich JA (1989). Bidirectional movement of actin filaments along tracks of myosin heads. *Nature* **341,** 154-156.

111. Uyeda TQ, Abramson PD & Spudich JA (1996). The neck region of the myosin motor domain acts as a lever arm to generate movement. *Proc Natl Acad Sci USA* **93,** 4459-4464.

112. Uyeda TQ, Kron SJ & Spudich JA (1990). Myosin step size. Estimation from slow sliding movement of actin over low densities of heavy meromyosin. *J Mol Biol* **214,** 699-710.

113. Veigel C, Bartoo ML, White DC, Sparrow JC & Molloy JE (1998). The stiffness of rabbit skeletal actomyosin cross-bridges determined with an optical tweezers transducer. *Biophys J* **75,** 1424-1438.

114. Veigel C, Coluccio LM, Jontes JD, Sparrow JC, Milligan RA & Molloy JE (1999). The motor protein myosin-I produces its working stroke in two steps. *Nature* **398,** 530-533.

115. Veigel C, Molloy JE, Schmitz S & Kendrick-Jones J (2003). Load-dependent kinetics of force production by smooth muscle myosin measured with optical tweezers. *Nat Cell Biol* **5,** 980-986.

116. Way M, Gooch J, Pope B & Weeds AG (1989). Expression of human plasma gelsolin in *Escherichia coli* and dissection of actin binding sites by segmental deletion mutagenesis. *The J Cell Biol* **109,** 593-605.

117. Weiss S, Rossi R, Pellegrino MA, Bottinelli R & Geeves MA (2001). Differing ADP release rates from myosin heavy chain isoforms define the shortening velocity of skeletal muscle fibers. *J Biol Chem* **276,** 45902-45908.

118. White HD & Taylor EW (1976). Energetics and mechanism of actomyosin adenosine triphosphatase. *Biochemistry* **15,** 5818-5826.

119. Woledge RC, Curtin NA & Homsher E (1985). Energetic aspects of muscle contraction. Academic Press London.

120. Yanagida T, Nakase M, Nishiyama K & Oosawa F (1984). Direct observation of motion of single F-actin filaments in the presence of myosin. *Nature* **307,** 58-60.